

Inward rectifier potassium channels interact with calcium channels to promote robust and physiological bistability

Title Page

Abbreviated title (50 character max): Kir and Ca channels promote robust bistability

Author Names and Affiliations: Anaëlle De Worm¹, Guillaume Drion^{1,*}, Pierre Sacré^{1,*}

¹Department of Electrical Engineering and Computer Science, University of Liège, Liège, Belgium

*These authors have contributed equally to this work.

Corresponding author's name and email address: Anaëlle De Worm (anaelle.deworm@uliege.be)

Number of pages: 34

Number of figures: 9

Number of Words

Abstract: 242

Introduction: 646

Discussion: 1016

Conflict of interest statement: The authors declare no competing financial interests.

Acknowledgements: Computational resources have been provided by the Consortium des Équipements de Calcul Intensif (CÉCI), funded by the Fonds de la Recherche Scientifique de Belgique (F.R.S.-FNRS) under Grant No. 2.5020.11 and by the Walloon Region. This work was supported by the Belgian Government through the Federal Public Service Policy and Support.

Abstract (250 Words Maximum)

In the dorsal horn, projection neurons play a significant role in pain processing by transmitting sensory stimuli to supraspinal centers during nociception. Following exposure to intense noxious stimuli, a sensitization process occurs to adapt the dorsal horn functional state. Notably, projection neurons can display a switch in firing pattern from tonic firing to plateau potentials with sustained afterdischarges. For afterdischarges to manifest after this switch, the neuron must develop bistability, which characterizes the ability to show resting or spiking at the same input current depending on the context. In numerous instances, neuronal bistability arises through voltage-gated calcium channels. However, computational studies have demonstrated a trade-off between bistability and the plausibility of its resting states if calcium channels are counterbalanced with voltage-gated potassium channels. Current knowledge leaves a gap in understanding the underlying mechanisms by which robust bistability, plateau potentials, and sustained afterdischarges emerge in neurons via calcium channels. In this study, we used a conductance-based model to explore the mechanisms by which L-type calcium (CaL) channels can achieve bistability when combined with either M-type potassium (KM) channels or inward-rectifying potassium (Kir) channels. Unlike KM channels, Kir channels enhance bistability. Combined with CaL channels, KM and Kir channels promote different types of bistability, with distinct robustness, and function. An analysis of their inward/outward properties revealed that their distinct steady-state currents explain this contrast. Altogether, the complementarity of CaL and Kir channels creates a reliable possible pathway for central sensitization in the dorsal horn.

Significant Statement (120 Words Maximum)

Neuronal bistability underlies short-term memory in neurons associated with sleep rhythms, motor control, working memory, epilepsy, schizophrenia, or pain amplification. At the single-cell level, bistability may emerge through the upregulation of voltage-gated calcium channels. Still, this phenomenon requires additional channels, such as voltage-gated potassium channels, to manifest within physiological ranges. In this context, however, a trade-off exists between bistability and the plausibility of its resting potentials, making it unclear how robust bistability appears physiologically. Using a conductance-based model, we explored how M-type or inward rectifier potassium channels combined with L-type calcium channels influence bistability. Our findings demonstrate that bistability may rely on ion channels interactions that bypass the aforementioned trade-off and promote distinct features relevant to neuronal processing.

Introduction (650 Words Maximum)

Nociceptive pain is a fundamental physiological sensation that protects the body integrity against noxious stimuli to avoid tissue damage (Woolf (2010)). In the event of a significant increase in threat intensity, sensitization triggers functional changes within the nociceptive system (Latremoliere and Woolf (2009)). These changes facilitate the triggering of pain and promote the subsequent recovery process. Dorsal horn projection neurons are a critical relay for sensory input to be transmitted to supraspinal centers during nociception. A subset of mechanisms contributing to sensitization target projection neurons, rendering them hyperexcitable and thus amplifying nociception (Reali and Russo (2005); Monteiro et al. (2006); Zain and Bonin (2019)). In particular, deep dorsal horn projection neurons exhibit an excitability switch under a change in modulatory inputs. More specifically, projection neurons can switch from tonic firing to plateau potentials with sustained afterdischarges (Derjean et al. (2003)). These afterdischarges are a sign of hyperexcitability of fundamental importance because they represent a substantial flow of information sent to supraspinal centers, triggering hyperalgesia and indicating a profound change in the sensory signal transmission properties (Cata et al. (2006); Monteiro et al. (2006); Robinson et al. (2014)). Indeed, afterdischarges extend the response to noxious stimuli by sustaining spiking following its end rather than reverting to a resting state—a feature commonly designated by bistability (Monteiro et al. (2006)).

Neuronal bistability has been the subject of investigation in several different neuronal populations (Lee and Heckman (1998); Kazantsev and Asatryan (2011); Dovzhenok and Kuznetsov (2012); Engbers et al. (2013); Franci et al. (2013); Borges et al. (2023)). However, the mechanisms by which robust and physiological bistability emerges in neurons at the single-cell level are not fully understood. Computational studies revealed that bistability between a resting and a spiking state may arise with a targeted increase in voltage-gated calcium channel conductance (Crunelli et al. (2005); Le et al. (2006); Borges et al. (2023)), but this must be combined with voltage-gated potassium channels to compensate for the induced hyperpolarization of resting potentials. However, classical voltage-gated potassium channels also have the side effect of significantly reducing the level of bistability (Yuen et al. (1995); Franci et al. (2013); Naudin et al. (2023)). This leads to a trade-off between bistability robustness and resting potential rectification. Conversely, an increasing body of work showed that the inward rectifier potassium (Kir) channels, a particular type of voltage-gated potassium channels can induce bistability (Shoemaker (2011); Sanders et al. (2013); Amarillo et al. (2018); Delmoe and Secomb (2023)). Evidence indicated that Kir channels are also present in superficial and deep projection neurons in the dorsal horn (Derjean et al. (2003); Murata et al. (2016); Ford and Baccei (2016); Malcangio (2018); Brewer and Baccei (2018)). Nevertheless, the impact of the interplay between Kir and calcium channels in diverse proportions on bistability remains to be elucidated, as do

the underlying mechanisms involved.

In light of this, we examined how the level of bistability changes in response to simultaneous increases in the conductance of L-type calcium (CaL) channels and the conductance of either the M-type potassium (KM) channels—a classical type of voltage-gated potassium channels—or the Kir channels, in a neuron with a reduced set of additional ion channels. For this purpose, we used a conductance-based model to determine how these two couples of ion channels affect bistability and reveal the mechanisms involved in each case. This approach demonstrated that, when coupled with CaL channels, Kir channels enhance bistability between resting and spiking, which is not observed with KM channels. Additionally, our results indicated that these distinct couples of voltage-gated ion channels give rise to two types of bistability that differ in robustness to intrinsic variability and noisy input currents. The contrasted shapes of the Kir and KM steady-state currents justified these differences. Finally, we explored the excitability switches that emerge when CaL channels are combined with either Kir or KM channels, and provided a computational explanation for the distinct robustness observed.

Materials and Methods

Conductance-based modeling

In this study, we used a single-compartment Hodgkin-Huxley model to characterize the excitability of a neuron. This method consists of computing the evolution of the membrane potential V in response to a given applied current I_{app} as:

$$C \frac{dV}{dt} = -I_{\text{leak}} - \sum_{\text{ion} \in \mathcal{I}} I_{\text{ion}} + I_{\text{app}},$$

where C is the membrane capacitance, I_{leak} is the leak current, I_{ion} are the intrinsic ionic currents with \mathcal{I} the set of all ionic channels. In this work, only voltage-dependent ion channels are considered, and each ionic current is defined by:

$$I_{\text{ion}} = \bar{g}_{\text{ion}} m_{\text{ion}}^{p_{\text{ion}}} h_{\text{ion}}^{q_{\text{ion}}} (V - E_{\text{ion}}),$$

where \bar{g}_{ion} denotes the ion channels maximal conductance, m_{ion} and h_{ion} correspond to the voltage-dependent activation and inactivation gates of the ion channels, p_{ion} is an integer between 1 and 4, q_{ion} is an integer between 0 and 1, and E_{ion} denotes the Nernst potential of the considered ionic current. The evolutions of the activation and

inactivation gates of a given ion channel are defined as:

$$\frac{dm_{\text{ion}}}{dt} = (m_{\text{ion},\infty}(V) - m_{\text{ion}}) / \tau_{m_{\text{ion}}}(V),$$

$$\frac{dh_{\text{ion}}}{dt} = (h_{\text{ion},\infty}(V) - h_{\text{ion}}) / \tau_{h_{\text{ion}}}(V),$$

where $m_{\text{ion},\infty}(V)$ and $h_{\text{ion},\infty}(V)$ denote the steady-state values of the activation and inactivation gates at a given membrane potential V , and $\tau_{m_{\text{ion}}}(V)$ and $\tau_{h_{\text{ion}}}(V)$ the time constants of the activation and inactivation gates at a given membrane potential V , respectively.

The ionic currents considered here consist of a voltage-gated fast sodium current I_{Na} , a slow delayed rectifier potassium current I_{KDR} , a L-type calcium current I_{CaL} , a M-type potassium current I_{KM} , an inward rectifier potassium current I_{Kir} , and a leak current I_{leak} . The model of I_{Na} and I_{KDR} was based on [Destexhe et al. \(1994\)](#). Each time constant, steady-state activation, and inactivation (when relevant) characterizing the evolution of the other ionic currents listed can be found in [Table 1](#). The nominal values of the fixed parameters are in [Table 2](#).

x_{ion}	$x_{\text{ion},\infty}(V)$	$\tau_{x_{\text{ion}}}(V)$
m_{CaL}	$\frac{1}{1 + \exp(-(V + 66.4565)/4)}$	$\frac{160}{\frac{0.1(-V-40)}{\exp(0.1(-V-40))-1+4 \exp((-V-65)/18)}}$
h_{CaL}	$\frac{1}{1 + \exp((V + 54)/4.03)}$	10000
m_{Kir}	$\frac{1}{1 + \exp((V + 65)/10)}$	10
m_{KM}	$\frac{1}{1 + \exp((-V - 76.1)/25.7)}$	103

Table 1: Steady-state activations and inactivation used to model I_{CaL} , I_{Kir} , and I_{KM} .

C	E_{Na}	E_{K}	E_{Ca}	E_{leak}	\bar{g}_{Na}	\bar{g}_{KDR}	\bar{g}_{leak}
1 $\mu\text{F}/\text{cm}^2$	50 mV	-90 mV	120 mV	-60.1 mV	30 mS/cm ²	4 mS/cm ²	0.033 mS/cm ²

Table 2: Nominal values of the fixed parameters of the conductance-based model.

Software

The model and all the following simulations and experiments were performed in the Julia programming language.

The code and packages used in this work will be made available on GitHub.

Current step and current pulse simulations

A time-dependent applied current was used to observe the neuron response to a current step and pulse. To create a step of current, the time dependency was introduced such that the applied current I is equal to:

$$I(t) = I_{s0} + (I_{s1} - I_{s0})H(t - t_{\text{step}}),$$

where $H(x)$ is the unit step function such that it equals 1 if $x \geq 0$ and 0 if $x < 0$. This current step was depolarizing when $I_{s1} > I_{s0}$ and hyperpolarizing otherwise.

To create a pulse of current, the time dependency was introduced such that the applied current I is equal to:

$$I(t) = I_{p0} + (I_{p1} - I_{p0})[H(t - t_{p,\text{starts}}) - H(t - t_{p,\text{ends}})],$$

meaning that this current pulse was depolarizing when $I_{p1} > I_{p0}$ and hyperpolarizing otherwise.

In Fig. 1A, we applied four hyperpolarizing steps of current at $t_{\text{step}} = 350$ ms with $I_{s0} = -3.19 \mu\text{A}/\text{cm}^2$ and I_{s1} taking one of the four values in the ensemble $\{-2.486; -1.783; -1.079; -0.375\} \mu\text{A}/\text{cm}^2$ from bottom to top.

In Fig. 1B, we applied four depolarizing steps of current at $t_{\text{step}} = 350$ ms with $I_{s0} = 0.328 \mu\text{A}/\text{cm}^2$ and I_{s1} taking one of the four values in the ensemble $\{-2.486; -1.783; -1.079; -0.375\} \mu\text{A}/\text{cm}^2$ from bottom to top.

For Figs. 1A and 1B, we used $\bar{g}_{\text{CaL}} = 0.03 \text{ mS}/\text{cm}^2$ and $\bar{g}_{\text{KM}} = \bar{g}_{\text{Kir}} = 0$.

In Fig. 2A, we applied a depolarizing pulse of current from $t_{p,\text{starts}} = 200$ ms to $t_{p,\text{ends}} = 600$ ms with $I_{s0} = -1.75 \mu\text{A}/\text{cm}^2$ and $I_{s1} = 0.9 \mu\text{A}/\text{cm}^2$ to the model defined with the set of maximal conductances: $\bar{g}_{\text{CaL}} = 0.03 \text{ mS}/\text{cm}^2$, $\bar{g}_{\text{KM}} = 0.1 \text{ mS}/\text{cm}^2$, and $\bar{g}_{\text{Kir}} = 0 \text{ mS}/\text{cm}^2$. In Fig. 2D, the same depolarizing pulse of current was adapted such that $I_{s0} = -1.65 \mu\text{A}/\text{cm}^2$ and $I_{s1} = 1 \mu\text{A}/\text{cm}^2$ to the model defined with the set of maximal conductances: $\bar{g}_{\text{CaL}} = 0.03 \text{ mS}/\text{cm}^2$, $\bar{g}_{\text{KM}} = 0 \text{ mS}/\text{cm}^2$, and $\bar{g}_{\text{Kir}} = 0.1 \text{ mS}/\text{cm}^2$.

In Fig. 3A, we applied two depolarizing pulses of current of similar amplitude both from $t_{p,\text{starts}} = 1000$ ms to $t_{p,\text{ends}} = 1500$ ms, first with $I_{s0} = -0.317 \mu\text{A}/\text{cm}^2$ and $I_{s1} = 0.683 \mu\text{A}/\text{cm}^2$ (Fig. 3A, top) and subsequently with $I_{s0} = 1.336 \mu\text{A}/\text{cm}^2$ and $I_{s1} = 2.336 \mu\text{A}/\text{cm}^2$ (Fig. 3A, bottom). The maximal conductance \bar{g}_{KM} was equal to $0.1 \text{ mS}/\text{cm}^2$ (Fig. 3A, top) or $0.2 \text{ mS}/\text{cm}^2$ (Fig. 3A, bottom), while \bar{g}_{CaL} and \bar{g}_{Kir} were constants to $0.023 \text{ mS}/\text{cm}^2$ and $0 \text{ mS}/\text{cm}^2$, respectively. In Fig. 3D, we applied two depolarizing pulses of current of similar amplitude both from $t_{p,\text{starts}} = 1000$ ms to $t_{p,\text{ends}} = 1500$ ms, first with $I_{s0} = -0.773 \mu\text{A}/\text{cm}^2$ and $I_{s1} = 0.977 \mu\text{A}/\text{cm}^2$ (Fig. 3D, top) and subsequently with $I_{s0} = 0.379 \mu\text{A}/\text{cm}^2$ and $I_{s1} = 2.129 \mu\text{A}/\text{cm}^2$ (Fig. 3D, bottom). The

maximal conductance \bar{g}_{Kir} was equal to 0.1 mS/cm^2 (Fig. 3D, top) or 0.2 mS/cm^2 (Fig. 3D, bottom), while \bar{g}_{CaL} and \bar{g}_{KM} were constants to 0.023 mS/cm^2 and 0 mS/cm^2 , respectively. The baseline current values in each figure were chosen so that the pulse average value lies at $2/3$ of the bistable window corresponding to each set of conductances under consideration.

In Fig. 8A, we applied an hyperpolarizing step of current at $t_{\text{step}} = 5 \text{ s}$ with $I_{s0} = 0.447 \mu\text{A/cm}^2$ and $I_{s1} = 0.427 \mu\text{A/cm}^2$. In Fig. 8C, we applied an hyperpolarizing step of current at $t_{\text{step}} = 5 \text{ s}$ with $I_{s0} = -0.356 \mu\text{A/cm}^2$ and $I_{s1} = -0.376 \mu\text{A/cm}^2$. In both cases, those values were chosen such that $I_{s0} = I_1 + 10 \text{ nA/cm}^2$ and $I_{s1} = I_1 - 10 \text{ nA/cm}^2$, to observe the neuron behavior around I_1 , the current at which spiking appears, for the set of maximal conductances chosen. The sets of maximal conductances chosen were $\{\bar{g}_{\text{CaL}}; \bar{g}_{\text{KM}}; \bar{g}_{\text{Kir}}\} = \{0; 0; 0.05\} \text{ mS/cm}^2$ in Fig. 8A and $\{\bar{g}_{\text{CaL}}; \bar{g}_{\text{KM}}; \bar{g}_{\text{Kir}}\} = \{0.01; 0; 0.05\} \text{ mS/cm}^2$ in Fig. 8C.

In Fig. 9A, we applied an hyperpolarizing step of current at $t_{\text{step}} = 5 \text{ s}$ with $I_{s0} = 0.128 \mu\text{A/cm}^2$ and $I_{s1} = 0.108 \mu\text{A/cm}^2$. In Fig. 9B, we applied an hyperpolarizing step of current at $t_{\text{step}} = 5 \text{ s}$ with $I_{s0} = 0.723 \mu\text{A/cm}^2$ and $I_{s1} = 0.703 \mu\text{A/cm}^2$. In both cases, those values were chosen such that $I_{s0} = I_1 + 10 \text{ nA/cm}^2$ and $I_{s1} = I_1 - 10 \text{ nA/cm}^2$, to observe the neuron behavior around I_1 , the current at which spiking appears, for the set of maximal conductances chosen. The set of maximal conductances chosen was $\{\bar{g}_{\text{CaL}}; \bar{g}_{\text{KM}}; \bar{g}_{\text{Kir}}\} = \{0.007; 0.048; 0\} \text{ mS/cm}^2$ in Fig. 9A and $\{\bar{g}_{\text{CaL}}; \bar{g}_{\text{KM}}; \bar{g}_{\text{Kir}}\} = \{0.007; 0.077; 0\} \text{ mS/cm}^2$ in Fig. 9B.

Computation of the fi curves

A frequency-current (fi) curve represents the steady-state spiking frequency observed at a constant applied current. In the context of a bistable neuron, an overlap exists between a zero-frequency state (*i.e.*, a resting state) and a non-zero-frequency state (*i.e.*, a spiking state) within a range of current values in which bistability is observed. In this work, we designate this range of current the *bistability window*, which is defined between the onset of spiking at current I_1 and the cessation of resting at I_2 .

Thus, the initial conditions used when computing the steady-state spiking frequency for currents within the bistability window must allow the neuron to converge to its spiking state. To determine them, we initialized the neuron at resting and applied a depolarizing current step from the i^{th} current (in the range of current tested) to a higher current, out of the bistability window. Then, the final state observed was used as the initial conditions to simulate the i^{th} constant current and determine the corresponding steady-state spiking frequency. This ensures that the ultra-slow inactivation gate of calcium channels is still open, and facilitates the convergence towards spiking, even with low steady-state frequencies. The model is then simulated for windows of 80 s until the spiking frequency

reaches steady-state. To compute the line of zero-frequency of the fI curve, we computed the model fixed points for the same range of current and incorporated a zero-frequency point if a stable fixed point was identified. The combination of these 2 computations was used in Fig. 1C (top) and Figs. 2B and E. In Fig. 1C (top), we used the maximal conductances: $\bar{g}_{CaL} = 0.03 \text{ mS/cm}^2$ and $\bar{g}_{KM} = \bar{g}_{Kir} = 0 \text{ mS/cm}^2$. The same maximal conductances were used for the grey data in Figs. 2B and E. However, the maximal conductance \bar{g}_{KM} was increased to 0.1 mS/cm^2 for the colored data in Fig. 2B, with $\bar{g}_{CaL} = 0.03 \text{ mS/cm}^2$ and $\bar{g}_{Kir} = 0 \text{ mS/cm}^2$. Similarly, the maximal conductance \bar{g}_{Kir} was increased to 0.1 mS/cm^2 for the colored data in Fig. 2E, with $\bar{g}_{CaL} = 0.03 \text{ mS/cm}^2$ and $\bar{g}_{KM} = 0 \text{ mS/cm}^2$.

In Fig. 1C (bottom), and Figs. 2C and F, we also represented the resting potential observed for the range of current used to display the fI curve. The resting potentials were computed together with the line of zero-frequency, by computing the membrane potential associated with the stable fixed point identified. The maximal conductances used in Figs. 1C (bottom), 2C and 2F were identical to the maximal conductances used in Figs. 1C (top), 2B and 2E, respectively.

Computation of the bistability window heatmaps

The computation of the fI curve is associated with a fixed set of conductances. To capture the evolution of the level of bistability, we varied the couple of maximal conductances, \bar{g}_{CaL} and either \bar{g}_{KM} or \bar{g}_{Kir} , and computed for each couple of conductances the (absolute) size of the bistability window, noted:

$$\Delta I = I_2 - I_1.$$

The current I_2 , which marks the end of the bistability window, was determined by identifying the highest current with a stable resting state. The stable resting states were computed using the same methodology to compute the fI curve zero-frequency line.

In contrast to the methodology employed in the computation of the descending fI curve, which determined the steady-state spiking frequency for each current within a specified range, in this instance, only the initial current, I_1 , situated at the beginning of the bistability window, was subjected to analysis. To compute I_1 for a given couple of conductances in a reasonable execution time, this algorithm was modified by employing an ascending range of current and initiated at a current from the resting-only regime. In this manner, the current I_1 was still identified as the lowest current at which spiking with a constant frequency can be observed over time intervals of 80 s, and with the same methodology employed to compute the neuron initial conditions (extracted from the end of a pulse

simulation). The results of this analysis are shown in Fig. 3B. In Fig. 3E, we performed the same experiment by varying the maximal conductance \bar{g}_{Kir} instead of \bar{g}_{KM} .

Similarly, the resting potential at the beginning of the bistability window (I_1) was determined as the membrane potential of the stable fixed point exhibited at I_1 , following the variation of either couple of conductances ($\bar{g}_{CaL}, \bar{g}_{KM}$) or ($\bar{g}_{CaL}, \bar{g}_{Kir}$). This methodology was used for Fig. 3C and Fig. 3F, respectively.

In Figs. 3E and 3F, we also represented a boundary denoting the excitability switch. The boundary in question was considered to have been crossed when the bistability window size became strictly positive, with the effective threshold used to create it being $\Delta I = 0.005 \mu A/cm^2$.

Response to noisy input currents

To evaluate the robustness of the resting and spiking states within the bistability window, which relies on either the couple ($\bar{g}_{CaL}, \bar{g}_{KM}$) or ($\bar{g}_{CaL}, \bar{g}_{Kir}$), we simulated the neuron response to a noisy input current superimposed to a constant current centered on the bistability window observed with the couple of conductances considered. For this purpose, the noisy current was generated as a piecewise constant process for which the value of each constant piece was sampled from a zero-mean Normal distribution, and the duration of each constant piece was fixed to 20 ms. In addition, the standard deviation of noise was varied incrementally between 10^{-3} and $10^{-1} \mu A/cm^2$.

In Figs. 4A, 4B, 4D and 4E, the standard deviation of the Normal distribution used to generate the superimposed noise was increased every 5 s and maintained at a constant level in time windows of 5 s, for a total simulation time of 50 s. In Figs. 4A and 4D, the set of initial conditions of the entire experiment was the resting state observed at the center of the bistability window of the couple of conductances considered (either ($\bar{g}_{CaL}, \bar{g}_{KM}$) or ($\bar{g}_{CaL}, \bar{g}_{Kir}$), respectively). Reciprocally, in Figs. 4B and 4E, the set of initial conditions of the entire experiment was a point of the spike trajectory obtained after applying the center of the bistability window of the couple of conductances considered (either ($\bar{g}_{CaL}, \bar{g}_{KM}$) or ($\bar{g}_{CaL}, \bar{g}_{Kir}$), respectively), without noise for 50 s, such that spiking has reached steady-state.

In Figs. 4C and 4F, we evaluated the global neuron ability to sustain either a resting or a spiking state in the presence of a fixed noise amplitude for each type of bistability, which was produced by coupling either ($\bar{g}_{CaL}, \bar{g}_{KM}$) or ($\bar{g}_{CaL}, \bar{g}_{Kir}$), respectively. To that end, a noisy applied current was sampled from a Normal distribution with a constant standard deviation throughout the simulation and simulated for a period of 50 s. This noisy current was then superimposed on the center current of the bistability window observed and applied to an initially resting (resp. spiking) neuron. If the neuron behavior transitioned to spiking (resp. resting) at the end of the simulation, a value

equal to 1 was stored as a marker of this state transition, and 0 otherwise. This experiment was repeated 500 times for each standard deviation value tested. The ability to sustain the initial behavioral pattern was quantified by the *proportion of state transition* and calculated as the mean value of the state transition markers recorded for each of the 500 simulations. Both Figs. 4C and 4F display the proportion of state transition given the constant standard deviation used to sample the noisy current when the neuron is initially spiking or resting. In Fig. 4C, bistability relies on the couple $(\bar{g}_{CaL}, \bar{g}_{KM})$ while in Fig. 4F, bistability relies on the couple $(\bar{g}_{CaL}, \bar{g}_{Kir})$.

The following set of maximal conductances was used in Figs. 4A, 4B, and 4C: $\bar{g}_{CaL} = 0.01 \text{ mS/cm}^2$, $\bar{g}_{KM} = 0.1 \text{ mS/cm}^2$, and $\bar{g}_{Kir} = 0 \text{ mS/cm}^2$. In Figs. 4D, 4E, and 4E, the following maximal conductances were used: $\bar{g}_{CaL} = 0.002 \text{ mS/cm}^2$, $\bar{g}_{KM} = 0 \text{ mS/cm}^2$, and $\bar{g}_{Kir} = 0.1 \text{ mS/cm}^2$.

Robustness to different levels of intrinsic variability

Each couple of conductances $(\bar{g}_{CaL}, \bar{g}_{KM})$ or $(\bar{g}_{CaL}, \bar{g}_{Kir})$ give rise to two types of bistability. We tested their robustness by measuring the relative change in the bistability window size ΔI for each couple considering neurons with heterogeneous intrinsic membrane properties.

To achieve this, three levels of intrinsic variability were introduced, comprising 10, 20, and 30 % in three parameters: the membrane capacitance C , the voltage-gated sodium channels maximal conductance \bar{g}_{Na} , and the leak conductance g_{leak} . Each parameter was randomly chosen in an interval centered on the corresponding nominal value used in the model. More specifically, in the case of a level of 10 % of variability, the membrane capacitance was sampled according to a uniform distribution from $C(1-0.1)$ to $C(1+0.1)$. The same procedure was repeated to sample \bar{g}_{Na} and g_{leak} . Subsequently, we computed I_1 and I_2 , the limits of the bistability window, using the same algorithm as for the bistability window heatmaps, and computed the relative change in the bistability window size ΔI to its nominal value. This computation was realized for both couples $(\bar{g}_{CaL}, \bar{g}_{KM})$ and $(\bar{g}_{CaL}, \bar{g}_{Kir})$. The results of the KM model (in purple tones) and the Kir model (in pink tones) in Fig. 5 were obtained with the sets of maximal conductances $\{\bar{g}_{CaL}; \bar{g}_{KM}; \bar{g}_{Kir}\} = \{0.023; 0.3; 0\} \text{ mS/cm}^2$ and $\{\bar{g}_{CaL}; \bar{g}_{KM}; \bar{g}_{Kir}\} = \{0.023; 0; 0.3\} \text{ mS/cm}^2$, respectively.

Computation of the steady-state currents and the differential conductances

Fig. 6 (top) illustrates the steady-state currents of I_{CaL} , I_{KM} , and I_{Kir} . At a given membrane potential, these steady-state currents are defined by the current amplitude with the activation and inactivation gates at steady-state, that is:

$$I_{ion,\infty}(V) = \bar{g}_{ion} (m_{ion,\infty}(V))^{p_{ion}} (h_{ion,\infty}(V))^{q_{ion}} (V - E_{ion}).$$

Based on this definition, the differential conductance shown in Fig. 6 (bottom) is the derivative of the steady-state current to the membrane potential ($\partial I_{\text{ion},\infty}/\partial V$) (method inspired from [Drion et al. \(2015\)](#)):

$$\begin{aligned} \frac{\partial I_{\text{ion},\infty}}{\partial V}(V) &= \bar{g}_{\text{ion}} (m_{\text{ion},\infty}(V))^{p_{\text{ion}}} (h_{\text{ion},\infty}(V))^{q_{\text{ion}}} \\ &+ \bar{g}_{\text{ion}} p_{\text{ion}} (m_{\text{ion},\infty}(V))^{p_{\text{ion}}-1} \frac{\partial m_{\text{ion},\infty}}{\partial V}(V) (h_{\text{ion},\infty}(V))^{q_{\text{ion}}} (V - E_{\text{ion}}) \\ &+ \bar{g}_{\text{ion}} (m_{\text{ion},\infty}(V))^{p_{\text{ion}}} q_{\text{ion}} (h_{\text{ion},\infty}(V))^{q_{\text{ion}}-1} \frac{\partial h_{\text{ion},\infty}}{\partial V}(V) (V - E_{\text{ion}}). \end{aligned}$$

The derivative of the activation and inactivation gates at steady-state were computed with an Euler method and plugged in the analytical expression above to compute $\partial I_{\text{ion},\infty}/\partial V$.

Analysis of the contribution of inward and outward currents

To investigate the reasons behind the differing impacts of KM and Kir channels on the level of bistability, we modified these channels separately to block their outward (resp. inward) currents. This approach allowed us to analyze the contribution of their inward (resp. outward) currents alone. The resulting inward currents flowing in these modified channels are designated by $I_{\text{KM},\text{inward}}$ and $I_{\text{Kir},\text{inward}}$, while the outward currents are denoted $I_{\text{KM},\text{outward}}$ and $I_{\text{Kir},\text{outward}}$. This modification is applied to the steady-state functions of the activation gates of both KM and Kir channels, both defined without an inactivation gate, realized as follows:

$$m_{\text{ion},\text{inward},\infty}(V) = \begin{cases} m_{\text{ion},\infty}(V), & \text{if } V \leq E_K, \\ 0, & \text{otherwise,} \end{cases} \quad \text{and} \quad m_{\text{ion},\text{outward},\infty}(V) = \begin{cases} m_{\text{ion},\infty}(V), & \text{if } V > E_K, \\ 0, & \text{otherwise.} \end{cases}$$

Fig. 7 (left) represents the steady-state inward and outward KM and Kir currents. To compute them, we replaced the steady-state activation gates previously used by their inward/outward form, defined above, in the definition of the steady-state currents. In Fig 7 (center), we represented the evolution of the bistability window limits (I_1 and I_2) as the maximal conductance of the current taken into account increased. The same methodology employed for the bistability window heatmaps was used to compute those limits. In Fig. 7 (right), we applied hyperpolarizing steps of currents to a neuron with a fixed maximal conductance for the current considered (*i.e.*, the inward KM current in the case of Fig. 7A (right)) from I_2 to I_1 , with $t_{\text{step}} = 200$ ms, starting from the resting state in I_2 , for a total time of 1 s. The maximal conductance \bar{g}_{CaL} used in Fig. 7 was 0.023 mS/cm².

Bifurcation analyses around the excitability switches

In Figs. 8B and D, and Fig. 9C, we represented a bifurcation diagram with respect to the applied current I for several sets of maximal conductances. To achieve this, the fixed points of the model were computed with the `NLsolve` package for each value of I that was tested. The computation of the limit cycle extrema, observed during spiking, at steady-state for a given constant applied current was based on the same methodology employed to compute the fI curves. Specifically, the results in Fig. 8B and in Fig. 8D relied on the set of maximal conductances $\{\bar{g}_{\text{CaL}}; \bar{g}_{\text{KM}}; \bar{g}_{\text{Kir}}\} = \{0.; 0.; 0.05\} \text{mS/cm}^2$ and $\{\bar{g}_{\text{CaL}}; \bar{g}_{\text{KM}}; \bar{g}_{\text{Kir}}\} = \{0.01; 0.; 0.05\} \text{mS/cm}^2$, respectively. The maximal conductances $\bar{g}_{\text{CaL}} = 0.007 \text{mS/cm}^2$ and $\bar{g}_{\text{Kir}} = 0 \text{mS/cm}^2$ were used in Fig. 9C, while \bar{g}_{KM} varied in between 0 and 0.1mS/cm^2 .

In Fig. 9D, we tracked the current at which a Saddle-Node (SN) bifurcation (I_{SN}) was observed according to the value of \bar{g}_{KM} considered. This was realized based on the fact that each SN bifurcation is a fixed point and that this fixed point should be an extrema of the IV curve, leading to a set of two equations:

$$\dot{V} = - \sum_{\text{ion} \in \mathcal{I}} I_{\text{ion}} + I = 0, \quad \frac{\partial \dot{V}}{\partial V} = 0.$$

Based on those results, we could find the value of \bar{g}_{KM} where the lower SN bifurcation collided with the inverse SN bifurcation and disappeared as observed in the bifurcation diagrams of Fig. 9C, and mark this particular event with a marker in Fig. 9D. This process was repeated for a range of value of \bar{g}_{CaL} to represent the boundary at which a possible excitability switch took place in Fig. 9E. The maximal conductances used in Fig. 9D were identical to those used in Fig. 9C.

Results

In this work, we used a conductance-based model to contrast the effect of the M-type (KM) and of the inward rectifier (Kir) potassium channels when coupled to L-type calcium (CaL) channels on bistability between resting and spiking states, which was either weakened or strengthened (respectively). Then, we point out the relevance of a couple of CaL and Kir channels for bistability by quantifying their robustness to noisy input currents and intrinsic variability using both types of potassium channels (KM or Kir) in combination with CaL channels. Next, we investigate how the features of the steady-state currents of CaL, KM, and Kir channels shape the ability to reinforce bistability and identify a region of negative differential conductance in the Kir current around the spike threshold, similar to that of the CaL current. To demonstrate that this feature is pivotal for strengthening bistability, we show

that the outward KM and Kir currents weaken and strengthen bistability respectively. In contrast, the inward KM and Kir currents do not interfere with bistability. Finally, we analyze the excitability switches created by CaL channels when coupled with either KM or Kir channels and relate these switches to bistability and plateau-type excitability.

In combination with CaL channels, KM channels weaken bistability, while Kir channels strengthen it.

When combined with fast voltage-gated sodium channels and slow delayed-rectifier potassium channels, voltage-gated calcium channels create bistability between resting and spiking, but at unrealistically low resting potentials. This effect is thought to be counterbalanced when calcium channels are coupled with voltage-gated potassium channels. However, common voltage-gated potassium channels do not solely rectify those equilibria, but weaken bistability. In this section, we illustrate this problem, first by adding L-type calcium (CaL) channels to a conductance-based model, creating unphysiological bistability, and then by adding M-type potassium (KM) channels, rectifying resting potentials at the cost of weakening bistability. Finally, we show that when adding instead a particular type of voltage-gated potassium channels, the inward rectifier potassium (Kir) channels, this trade-off does not exist, suggesting that those channels promote robust and physiological bistability when combined with calcium channels.

The addition of L-type voltage-gated calcium channels to a conductance-based model, including already a fast sodium current I_{Na} , a delayed-rectifier potassium current I_{KDR} and a leak current I_{leak} , enables the neuron to exhibit bistability. Indeed, both spiking and resting could be observed for a range of currents depending on the neuron's initial behavior. This feature was demonstrated by separately applying an ascending current step and a descending current step, with distinct initial currents, but both reaching an identical applied current. Starting at a low input current, the neuron was initially resting and switched to spiking only for large ascending steps of current (Fig. 1A, yellow), but maintained resting otherwise (Fig. 1A, purple and red tones). Reciprocally, starting at a high input current, the neuron displayed spiking and switched to resting only after the application of a descending step of current to the lowest value chosen (Fig. 1B, purple), and maintained spiking otherwise (Fig. 1A, yellow and red tones). Taken together, these results showed that the two center values of currents in the set of four tested could be associated with both resting or spiking depending on the initial neuron behavior (Fig. 1A, and Fig. 1B, red tones). The two other values were outside the range of currents in which both behaviors could be observed and displayed either resting or spiking (Fig. 1A, and Fig. 1B, purple and yellow, respectively). For each initial state (resting and spiking), the final steady-state spiking frequency and the final resting potential were computed to display the fI curve (Fig. 1C, top) and the corresponding equilibrium potentials $\bar{V}(I)$ as a function of the applied

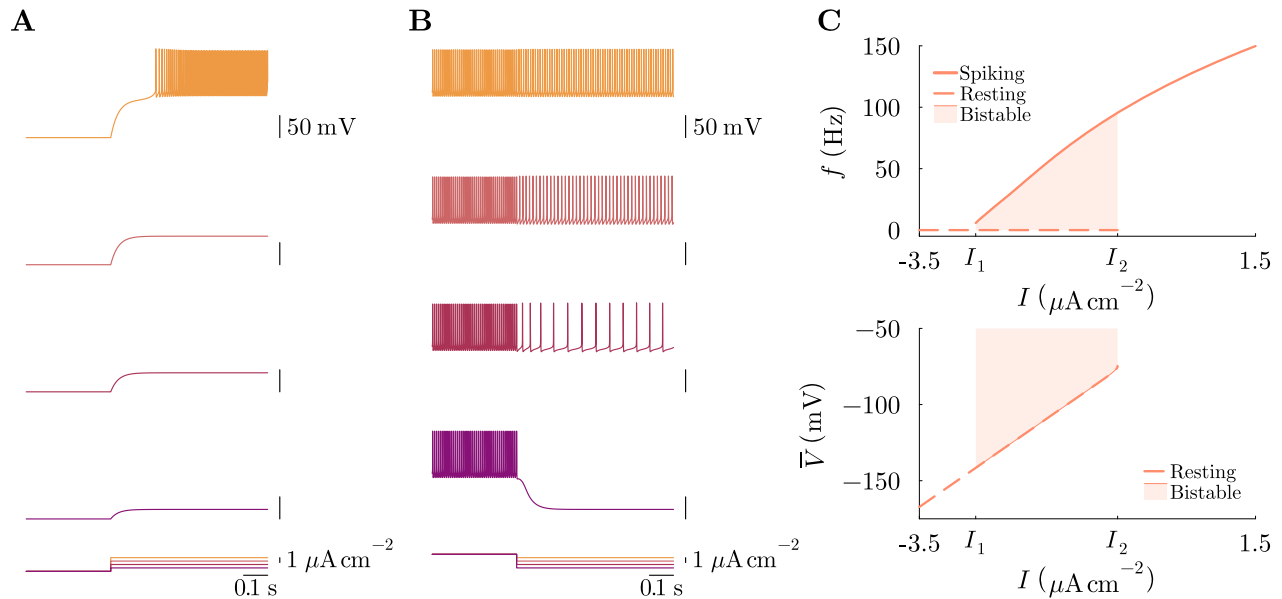


Figure 1: Voltage-gated calcium channels produce bistability—the capacity to display either resting or spiking at a given current value, depending on the initial conditions. **A**, When initially resting, the application of ascending steps of current with increasing amplitude results in a progressive depolarization of the membrane potential (purple and reds). At high current values, the neuron switches from resting to spiking (yellow). **B**, When initially spiking, the application of descending steps of current with increasing amplitude results in a progressive decrease of the firing frequency (yellow and reds). At low current values, the neuron switches from spiking to resting (purple). **C**, The superimposition of the fi curves computed from resting and spiking respectively identifies the bistability window (top), that is, the range of currents from I_1 to I_2 within which both resting or spiking can be observed, as for A and B, in reds. The resting equilibrium potentials within and below the bistability window are progressively depolarized as the current increases (bottom).

current (Fig. 1C, bottom). The bistable window created by calcium channels was well captured on the fi curve, where both resting (associated with a zero-frequency) and spiking were observed in a range of current delimited by I_1 and I_2 . Above I_2 , only spiking was observed. From I_1 to I_2 , both resting and spiking could be observed depending on the neuron’s initial conditions. Only resting was observed for currents below I_1 . However, the equilibrium potentials were unrealistically hyperpolarized, meaning that the switch from spiking to resting, from above to below I_1 , may not be physiological. Moreover, the size of the bistability window increased as the L-type calcium channel conductance (\bar{g}_{CaL}) increased, but this in turn created even more hyperpolarized resting potentials around I_1 (Supp. Fig 1). Taken together, these results demonstrated that calcium channels provide a high level of bistability but at unrealistically low equilibria, and that they must be combined with other types of ion channels to compensate for this lack of plausibility and create robust and physiological bistability.

In numerous instances, the increase in calcium channels conductance is assumed to be coupled with an increase in the conductance of low-threshold voltage-gated potassium channels to create physiological bistability. Such

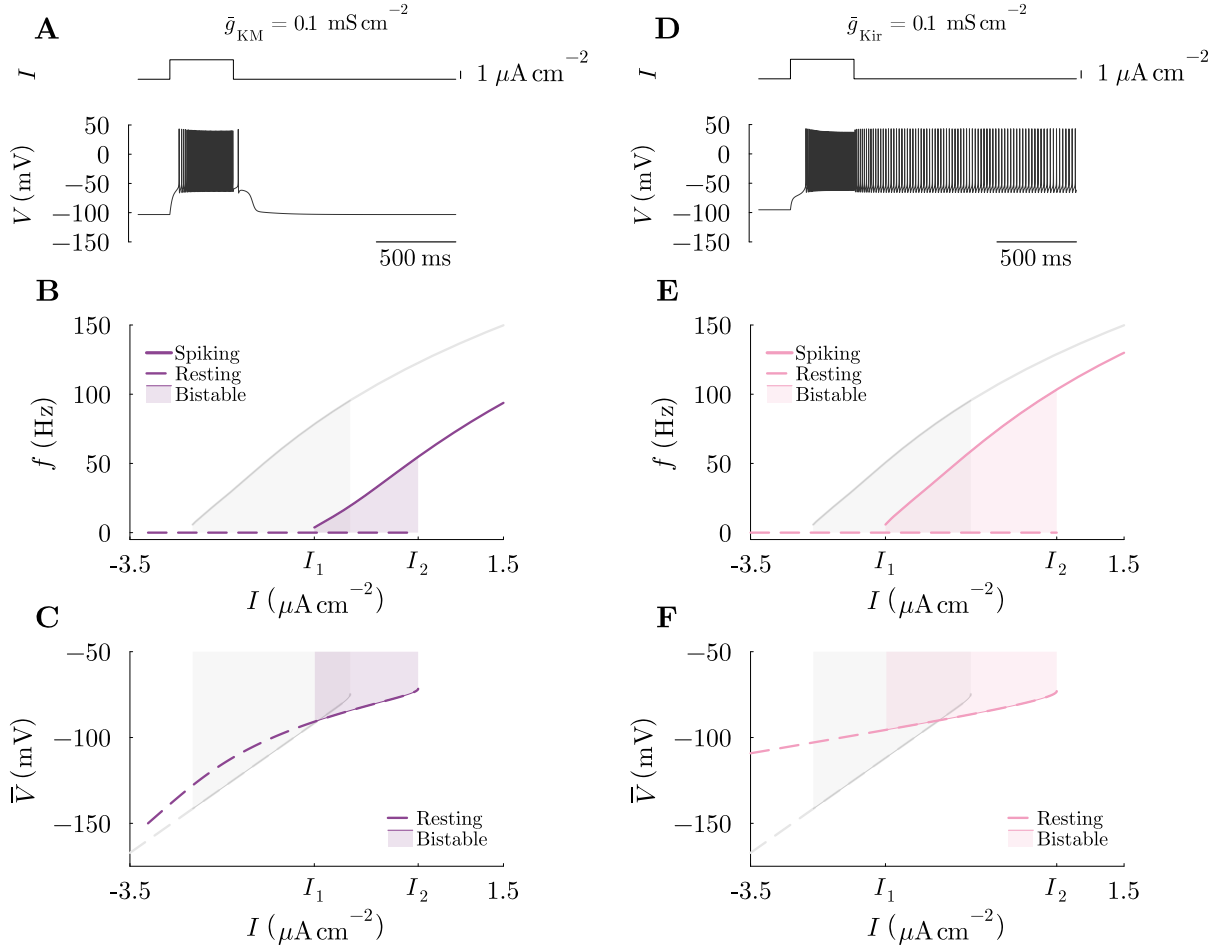


Figure 2: Depending on the added voltage-gated potassium channels, bistability is either maintained or weakened, while the resting potentials are more or less rectified. **A**, When adding a KM channel conductance \bar{g}_{KM} , the neuron pulse response shows bistability between resting and spiking for the baseline current used. **B**, The superimposed fI curves from resting and spiking show that the bistability window created by calcium channels (grey) is maintained after the addition of KM channels (pink). **C**, The unrealistically low resting membrane potentials (grey) are rectified by the addition of KM channels (pink). **D**, The pulse response of the neuron when KM channels are replaced by Kir channels shows that bistability is not observed for a similar pulse amplitude. **E**, The superimposed fI curves from resting and spiking show that the bistability window is smaller when calcium channels are combined with Kir channels (purple). **F**, The unrealistically low resting membrane potentials (grey) are slightly increased by the addition of Kir channels (purple).

a couple might improve the equilibrium potentials around I_1 by bringing them closer to physiological ranges. To illustrate how such a couple impacts bistability, we added an M-type potassium conductance (\bar{g}_{KM}) to the conductance-based model. When applying an input pulse of current of magnitude comparable to Fig. 1A and B, bistability could not be observed anymore, as the neuron did not maintain spiking once the pulse ended (Fig. 2A). As for the previous set of conductances, we computed the steady-state spiking frequency when the neuron was initially either spiking or resting for a large range of currents, and superimposed the two resulting fI curves (Fig. 2B).

The bistability window appeared much narrower following the addition of KM channels (Fig. 2B, purple shaded area) compared to the previous results, without KM channels (Fig. 2B, grey shaded area). However, computing the resting potentials for the same range of current demonstrated that KM channels slightly rectified these equilibrium potentials (Fig. 2C, purple) compared to the previous results, in the absence of KM channels (Fig. 2C, grey). Together, these two effects illustrated the trade-off faced with classical potassium channels: the higher the equilibrium potential rectification needs to be, the shorter the bistability window is. In other words, equilibrium potential rectification through KM channels works at the expense of weakening bistability, and may even make robust and physiological bistability incompatible.

Voltage-gated potassium channels family also includes a very special group of potassium channels: the inward rectifier potassium (Kir) channels. To determine their effect on bistability, the previously considered addition of a KM channels conductance was replaced by a Kir channels conductance (\bar{g}_{Kir}). After applying a pulse of current of the same amplitude as in Fig. 2A, bistability was retrieved in the neuron response (Fig. 2D). The superimposition of the two fI curves corresponding to either initial spiking or initial resting revealed that the addition of Kir channels preserved the size of the bistability window by shifting I_1 and I_2 (Fig. 2E, pink shaded area), compared to the previous results obtained without the addition of voltage-gated potassium channels (Fig. 2E, grey shaded area). Additionally, computing the equilibrium potentials for the same range of applied current showed that the resting potential rectification provided by Kir channels was very efficient. Therefore, the trade-off between the bistability window size and the plausibility of the resting potentials observed with KM channels disappeared when CaL channels were combined with Kir channels, suggesting that the latter couple promotes robust and physiological bistability.

With fixed values of conductances, we showed that when CaL and KM channels are coupled, a trade-off exists between the bistability window size and the resting potential rectification. Subsequently, we investigated how this trade-off evolved when the balance between these coupled conductances changed. To start this investigation, the model response to a pulse of current with a fixed \bar{g}_{CaL} , and two different values of \bar{g}_{KM} were simulated (Fig. 3A). The amplitude of the current pulses was identical across these two simulations. Additionally, the baseline current values were chosen such that the pulse average value lies at $2/3$ of the bistable window corresponding to each set of conductances under consideration. The neuron responses demonstrated that an increase in \bar{g}_{KM} narrowed the bistability window such that the neuron could not maintain continuous spiking after the pulse ended (Fig. 3A, top to bottom). Next, we explored the effect of several balances between \bar{g}_{CaL} and \bar{g}_{KM} on the resulting bistability window size (ΔI), defined as the absolute difference between I_1 and I_2 in the fI curves plot, and on the resting

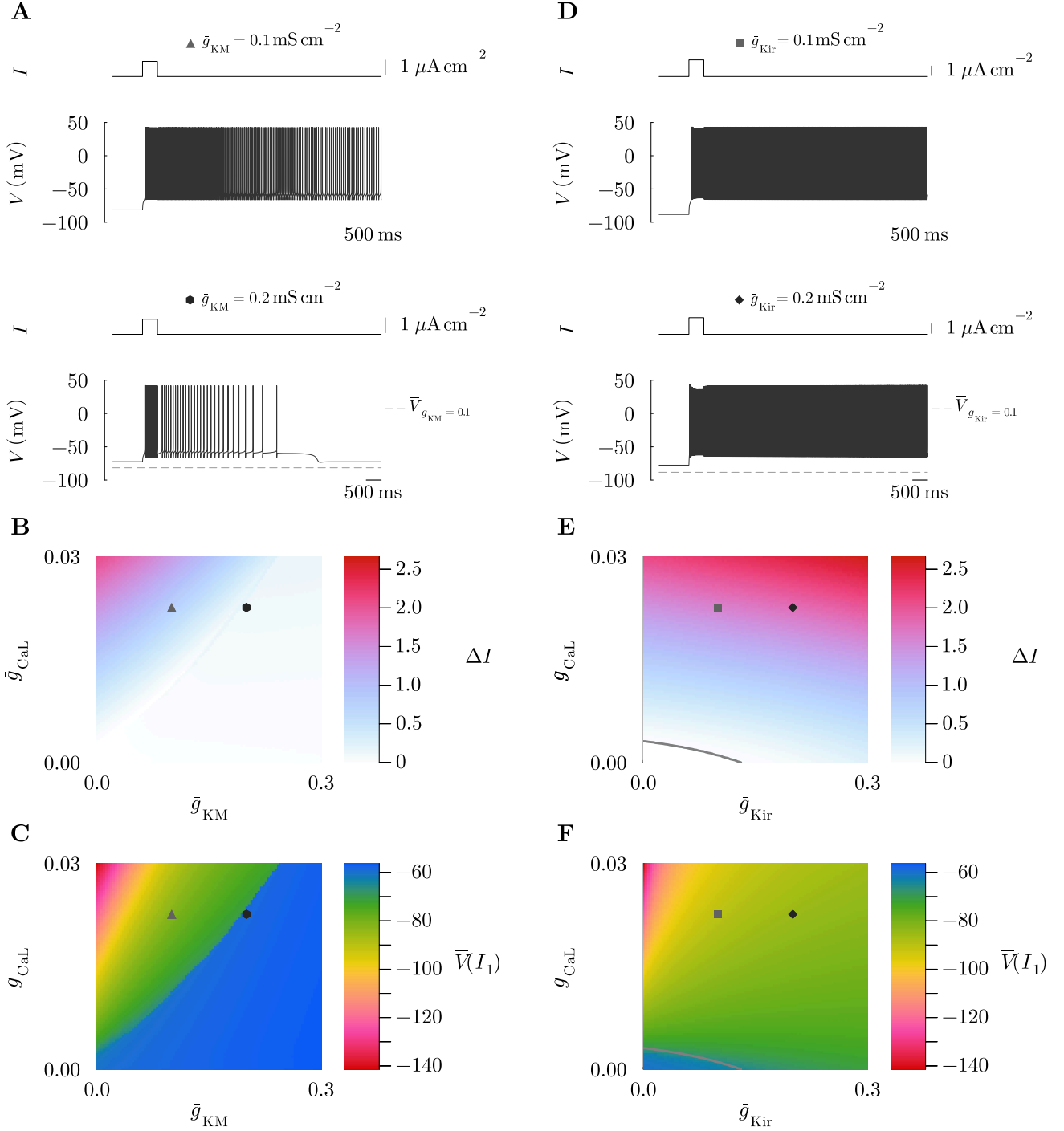
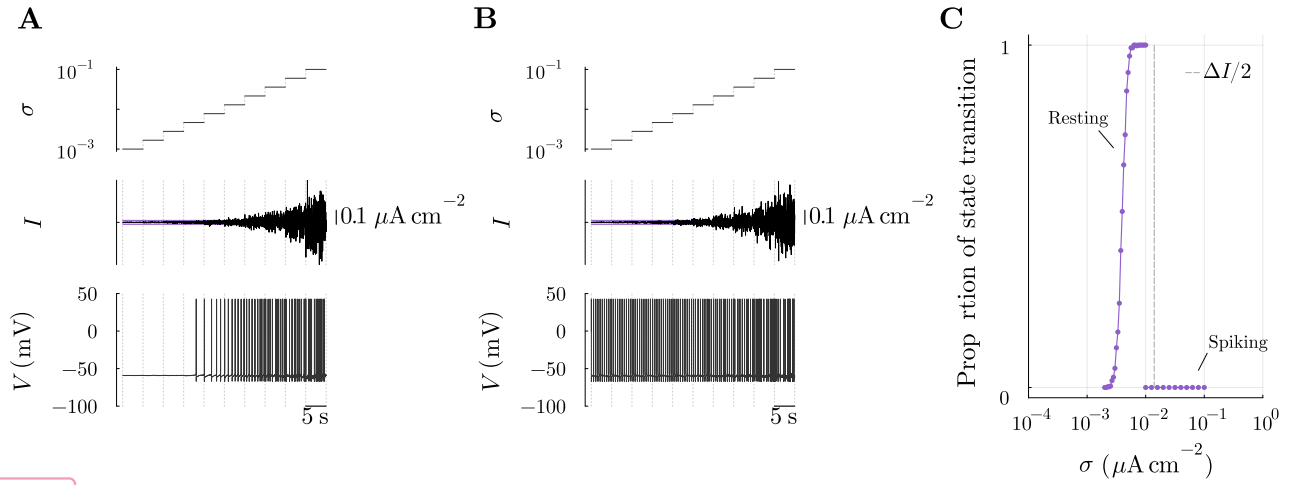


Figure 3: Resting potential rectification is improved by separately increasing the conductance of both voltage-gated potassium channels, but bistability is either strengthened or weakened depending on the type of potassium channels considered. **A**, After increasing the KM channels conductance (\bar{g}_{KM}), bistability is still observed in the pulse response (top to bottom). **B**, Heatmap of the bistability window size (ΔI), computed as the difference between I_2 and I_1 , depending on the pair of conductances (\bar{g}_{CaL} , \bar{g}_{KM}) used. **C**, Heatmap of the resting potential at the lower bound of the bistability window ($\bar{V}(I_1)$), depending on the pair of conductances (\bar{g}_{CaL} , \bar{g}_{KM}) used. **D**, After increasing the Kir channels conductance (\bar{g}_{Kir}), bistability is no longer observed in the pulse response, since spiking is not maintained after the pulse of current ends. **E**, Same as B, with a pair of conductances (\bar{g}_{CaL} , \bar{g}_{Kir}) used. **F**, Same as C, with a pair of conductances (\bar{g}_{CaL} , \bar{g}_{Kir}) used.

KM



Kir

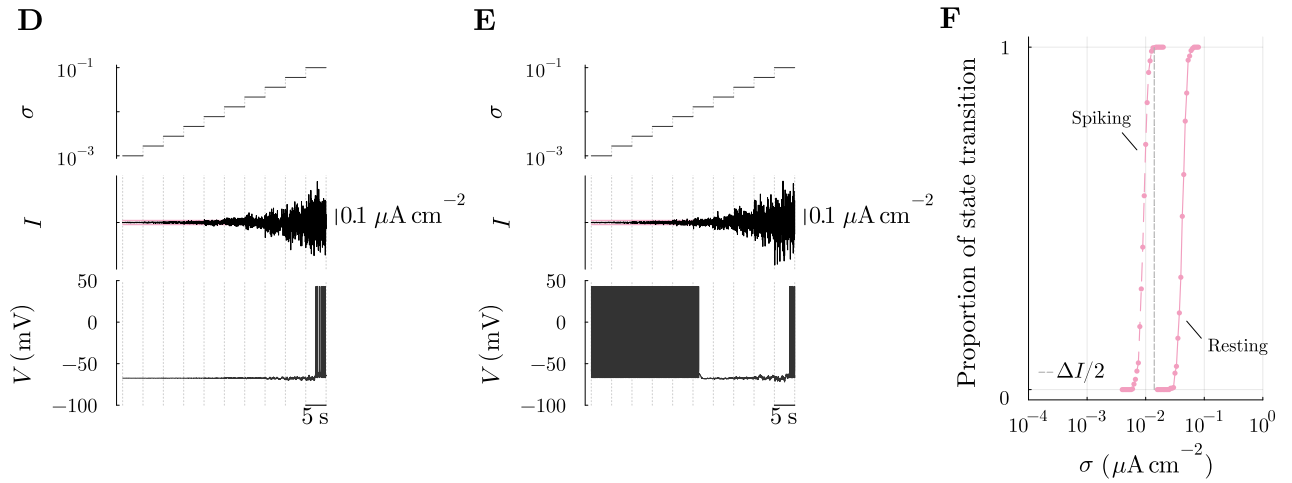


Figure 4: Depending on the voltage-gated potassium channels added, resting and spiking show distinct robustness to noise in the center of the bistability window. **A**, Response of the model including I_{KM} to the application of the central current of the bistability window with an additional Normal noise whose standard deviation (σ , expressed in $\mu\text{A}/\text{cm}^2$) increases every 5 seconds when initially resting. **B**, Same as **A**, when initially spiking. **C**, Proportion of trials that failed to maintain their initial behavior (resting or spiking) and transitioned to spiking or resting, respectively, as a function of the constant standard deviation used for the Normal noise superimposed on the central current. These results were also obtained using the model including I_{KM} . **D**, Same as **A**, but with the model including I_{Kir} instead of I_{KM} . **E**, Same as **A**, but with the model including I_{Kir} instead of I_{KM} , and when initially spiking. **F**, Same as **C**, but with the model including I_{Kir} instead of I_{KM} . The level of bistability in **A**, **B**, and **C**, (resulting from the addition of I_{KM}) is similar to those of **D**, **E**, and **F** (resulting from the addition of I_{Kir}). To achieve this similarity, we used a \bar{g}_{Kir} identical to the \bar{g}_{KM} in **D**, **E**, and **F**, and a reduced \bar{g}_{CaL} compared to the value used in **A**, **B**, and **C**.

potential at the beginning of each bistability window ($\bar{V}(I_1)$) (Figs. 3B and C, respectively). These results showed that KM channels highly narrowed the bistability windows created by calcium channels, achieving very low levels of bistability for large values of \bar{g}_{KM} (Fig. 3B). Nonetheless, a specific balance between \bar{g}_{CaL} and \bar{g}_{KM} gave rise

to a small reduction in bistability window size (Fig. 3B, blue area, with $\Delta I \approx 0.5 \mu\text{A}$) and an acceptable resting potential rectification in I_1 (Fig. 3C, green area, with $\bar{V}(I_1) \approx -75 \text{ mV}$), which illustrated the trade-off previously mentioned. However, such a specific balance between $(\bar{g}_{\text{KM}}, \bar{g}_{\text{CaL}})$ was close to a net shift in the resting potentials observed in I_1 , that increased suddenly by approximately 20 mV (Fig. 3C, dark blue area). This suggests that strong unbalances between \bar{g}_{CaL} and \bar{g}_{KM} can lead to an excitability switch in the neuron behavior, which is further detailed in a dedicated section.

Conversely, we showed that the trade-off between bistability window size and the resting potential rectification did not appear when KM channels were replaced by Kir channels. A similar analysis evaluated how these results evolved for various balances between CaL and Kir channels conductances. First, we considered a fixed \bar{g}_{CaL} and two values of \bar{g}_{Kir} , and applied current pulses of identical amplitude, with averaged values lying at 2/3 of each bistability window (Fig. 3D). This showed that bistability was maintained for an increase in \bar{g}_{Kir} , for a fixed \bar{g}_{CaL} . Next, we varied both \bar{g}_{CaL} and \bar{g}_{Kir} conductances and computed the resulting size of the bistability window (ΔI) (Fig. 3E), and the resting potential at the beginning of each bistability window ($\bar{V}(I_1)$) (Fig. 3F), for each set of conductances. For a given level of calcium channels conductance, an increase in Kir channels conductance not only maintained but also increased the size of the bistability window, while rectifying the corresponding resting potentials, even with particularly low calcium channels conductance. Consequently, the underlying mechanisms by which the couple of Kir and CaL channels creates robust and physiological bistability were very distinct from those emerging from the couple of KM and CaL channels, for which a considerably higher calcium channels conductance is necessary. This suggests that these two couples might trigger different types of excitability switches. In the context of the Kir and CaL channels couple, an excitability switch must occur when bistability appears (Fig. 3E, grey line, and Fig. 3F, grey line), as discussed in further sections. In the context of a couple of KM and CaL channels, the excitability switch is more complex to define and is also discussed in further sections.

Bistability is more robust to noisy inputs and intrinsic variability when CaL and Kir channels are combined.

For physiological bistability to arise, calcium channels must be coupled with other ion channels, such as voltage-gated potassium channels. However, depending on the type of voltage-gated potassium channels considered, we demonstrated that bistability was enhanced (Fig. 3E) or severely diminished (Fig. 3B) when the corresponding conductance increased. Additionally, the sudden shift in resting potentials in I_1 as the KM channels conductance increased (Fig. 3C, dark blue area) suggests that the weak bistability rising from the couple $(\bar{g}_{\text{KM}}, \bar{g}_{\text{CaL}})$ relies on a different type of excitability than the bistability emerging from the couple $(\bar{g}_{\text{Kir}}, \bar{g}_{\text{CaL}})$. Consequently, the characteristics of bistability may differ significantly depending on the couple considered. To address this issue,

this section investigates their robustness to noise and intrinsic variability separately.

First, to analyze the robustness to noise of both types of bistability, we chose two conductances sets ($\bar{g}_{CaL}, \bar{g}_{KM}$) and ($\bar{g}_{CaL}, \bar{g}_{Kir}$), with identical values of \bar{g}_{KM} and \bar{g}_{Kir} . The calcium channel conductance chosen in combination with Kir channels was reduced compared to the value used in combination with KM channels, to achieve similar bistability window sizes. Subsequently, we applied the central current of the bistability window of each couple and superimposed a Normal noise whose standard deviation (σ) increased with time. This analysis allowed us to determine how robust resting and spiking were according to both types of bistability, and whether one state was more robust than the other.

Considering the \bar{g}_{KM} -bistability, the initial resting state was rapidly corrupted by noise as the standard deviation increased (Fig 4A). For the first few tens of seconds, the equilibrium potential simply oscillated and followed the current variations caused by the Normal noise applied. Although this noisy current remained in the bistability window between 15 and 20 s, the membrane potential eventually left the resting state and transitioned to spiking. Conversely, the initial spiking state was never lost as the standard deviation increased (Fig 4B). Indeed, although the instantaneous spiking frequency was clearly affected by noise in the last tens of seconds, the neuron maintained spiking at the end of the simulation. This illustrated that spiking was very robust to noise, while small perturbations prevented the neuron from maintaining a resting state. Due to the probabilistic nature of the noise applied, using the same value of standard deviation to sample the noise twice may cause the neuron to leave the chosen initial state in the first trial, and maintain it in the second one. Therefore, to better capture the robustness of each behavior, we produced 500 trials where the noise superimposed to the center current of the bistability window was sampled using a constant value of standard deviation throughout each trial. In each set of 500 trials corresponding to only one value of standard deviation and only one possible initial state (*i.e.*, resting or spiking), we reported the proportion of trials that displayed a state transition (Fig 4C). These results showed that the resting state was maintained only for small perturbations, while spiking could always be carried on.

The same experiments can be performed with instead the combination of \bar{g}_{Kir} and \bar{g}_{CaL} to characterize the robustness of a comparable level of \bar{g}_{Kir} -bistability. Here, only large standard deviations elicited spiking when the neuron was initialized to its resting state, as shown in the last seconds of the experiment (Fig 4D). Slightly lower standard deviations caused the neuron to transition from spiking to resting (Fig 4E). Nevertheless, as the neuron could not maintain its resting state for even larger perturbations, the final few tens of seconds exhibited spiking. As a result, resting was more robust than spiking, since it could withstand higher standard deviations, even when applied constantly throughout trials (Fig 4F). Nevertheless, both spiking and resting in \bar{g}_{Kir} -bistability were more

robust than resting in \bar{g}_{KM} -bistability (Figs 4F and C, respectively).

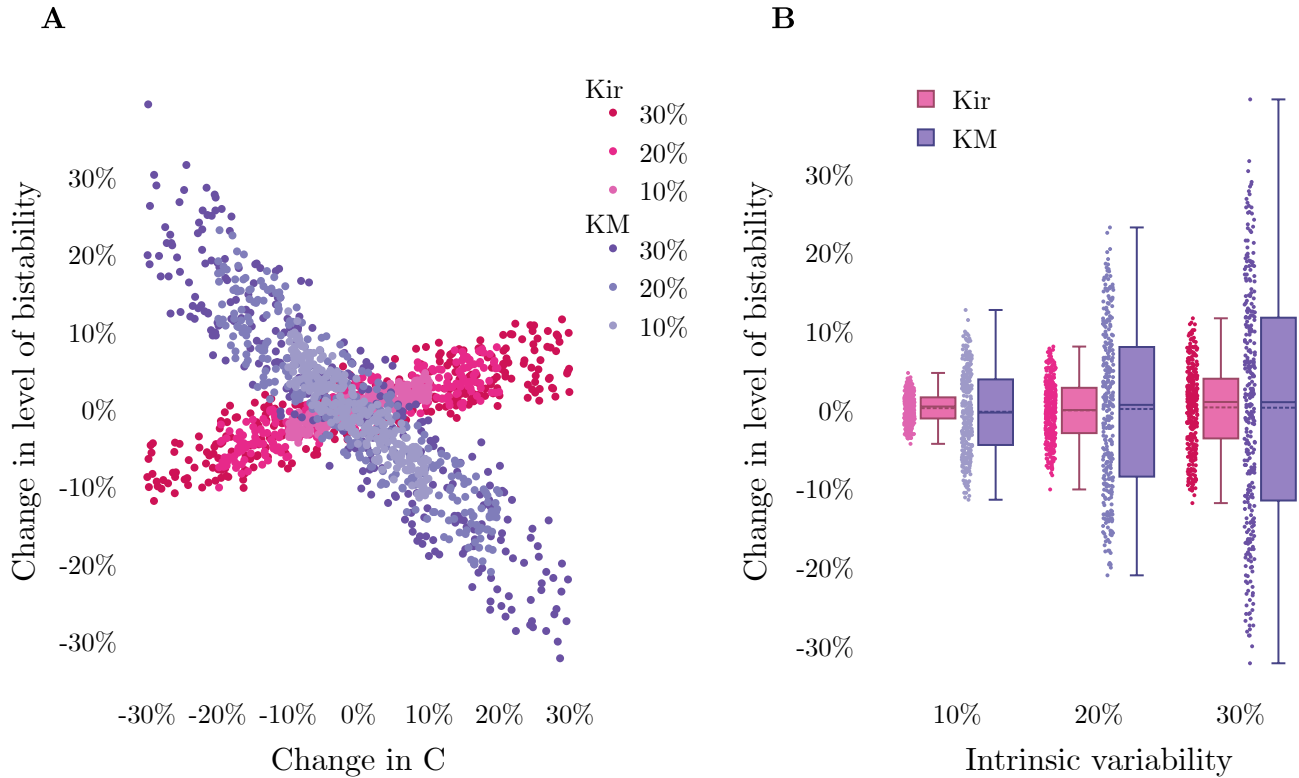


Figure 5: Addition of either Kir channels or KM channels leads to different relative robustness to intrinsic variability. **A**, Relative changes in the level of bistability after introducing 10 %, 20 %, and 30 % of intrinsic variability for the model with either Kir channels (pink shades) or KM channels (purple shades), as a function of the membrane capacitance used. **B**, Boxplot of the relative changes in the level of bistability after introducing 10 %, 20 %, and 30 % of intrinsic variability for each of these potassium channels.

Next, we investigated the robustness of both types of bistability to intrinsic variability. This allowed us to estimate how a given level of bistability, with fixed conductances ($\bar{g}_{CaL}, \bar{g}_{Kir}$) or ($\bar{g}_{CaL}, \bar{g}_{KM}$), evolved in heterogeneous neurons with different intrinsic properties. To this end, the membrane capacitance (C), the voltage-gated sodium channels conductance, and the leak conductance were sampled uniformly within an interval of $\pm 10\%$, $\pm 20\%$, or $\pm 30\%$, around their respective nominal values. The sets of conductances ($\bar{g}_{CaL}, \bar{g}_{Kir}$) and ($\bar{g}_{CaL}, \bar{g}_{KM}$) chosen for this analysis was identical and thus created different bistability window sizes. More specifically, \bar{g}_{Kir} and \bar{g}_{KM} were set to 0.3, while \bar{g}_{CaL} was set approximately to 0.025, for the \bar{g}_{KM} -bistability to remain in the dark blue area of Fig. 3F.

After introducing intrinsic variability with either \bar{g}_{Kir} -bistability or \bar{g}_{KM} -bistability, we computed the relative change in the bistability window size. These relative changes were defined in the high-dimensional space ($C, \bar{g}_{Na}, g_{leak}$), but those results were represented across the membrane capacitance (C) only, for each level of

intrinsic variability considered (Fig. 5A). A change in the membrane capacitance had opposite effects on each type of bistability, but to a lesser extent on \bar{g}_{Kir} -bistability compared to \bar{g}_{KM} -bistability. Indeed, for a given degree of intrinsic variability, the relative changes in \bar{g}_{KM} -bistability appeared to be around three times greater than those in \bar{g}_{Kir} -bistability, which was bounded in approximately $\pm 10\%$ (Fig. 5B).

Ion channels increasing bistability have a steady-state current exhibiting a region of negative differential conductance.

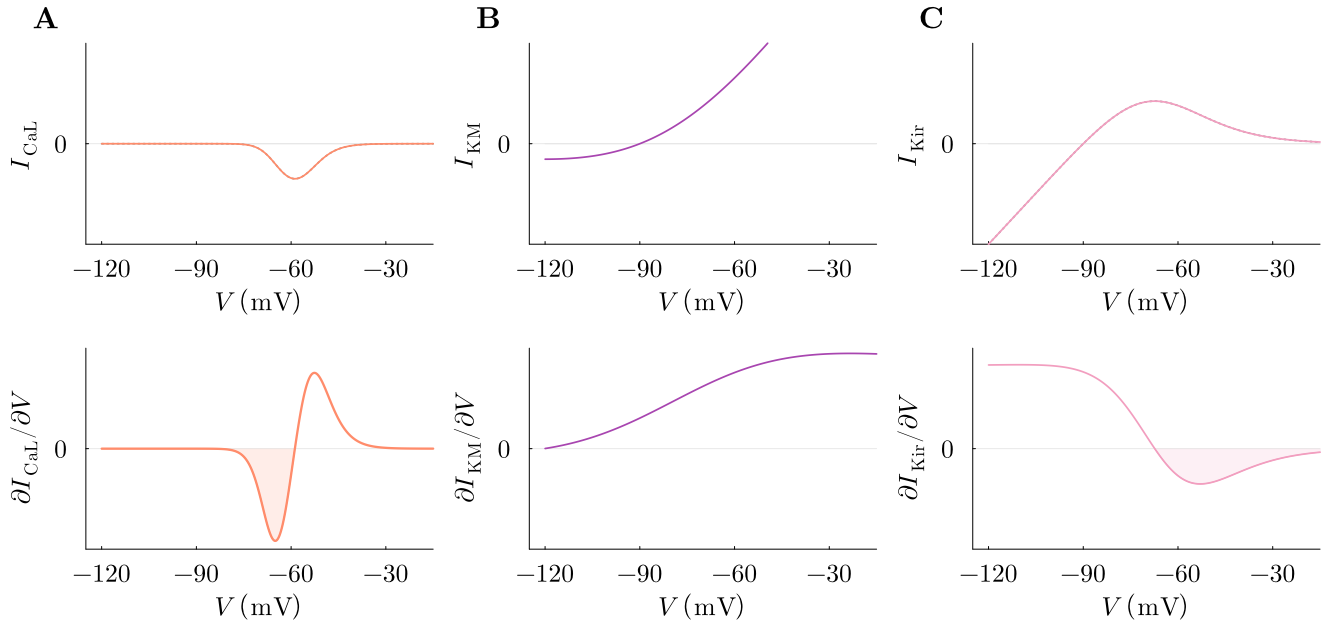


Figure 6: Steady-state currents of ion channels promoting bistability show local negative differential conductance around the spike threshold. **A**, Steady-state L-type calcium current I_{CaL} (top) and its differential conductance (bottom) for a range of membrane potentials. The region of negative differential conductance is highlighted by a shaded area. **B**, Same as A with the KM current I_{KM} . **C**, Same as A with the Kir current I_{Kir} , lacking a region of negative differential conductance.

Altogether, the addition of KM channels tended to impair bistability, while rectifying the corresponding range of equilibrium potentials (Figs. 3B and C). In contrast, adding Kir channels promoted physiological bistability (Fig. 3E and F). The mechanisms by which Kir and KM exert such disparate effects on the bistability window size remain unclear. As both channels are voltage-gated potassium channels and operate in a similar timescale, the main difference is the range of potentials at which they are opened. This range of openings inherently impacts the steady-state current flowing in these channels. This section compares the characteristics of the steady-state currents produced by each type of ion channels that alters the onset of physiological bistability.

Calcium channels produce an inward current (Fig. 6A, top) that creates bistability. This current is associated with a region of negative differential conductance near the spike threshold (about -65 mV) (Fig. 6A, bottom,

shaded area). Previous research indicated that this property of calcium channels is responsible for the onset of bistability (Franci et al. (2013); Drion et al. (2015)). As for common voltage-gated potassium channels, KM channels exhibit a small inward current and a strong outward current (Fig. 6B, top), that do not show any region of negative differential conductance (Fig. 6B, bottom).

Unlike classical voltage-gated potassium channels, Kir channels exhibit a strong inward current at potentials below their reversal potential E_K , and a small outward current above it (Fig. 6C, top). In analogy with the inward current that flows in calcium channels, the steady-state outward current that flows in Kir channels also displays a region of negative differential conductance around and above the spike threshold (Fig. 6C, bottom). In this range of potentials, a small increase in membrane potential around the spike threshold corresponds to a decrease in outward Kir current, which favors a further increase in membrane potential, and so on, which leads to spiking. Consequently, the sign of the differential conductance around the spike threshold could be an indicator of voltage-gated potassium channels' tendency to reduce or enhance bistability. If this is the case, blocking of the current around the spike threshold, and the induced removal of these regions of negative/positive differential conductance, may result in the removal of the decrease/increase in the bistability window size observed. This hypothesis is the subject of further investigation in the next section.

The inward currents rectify resting potentials and maintain bistability, but the outward potassium currents either increase or decrease bistability.

An increase in the calcium channels conductance led to an expansion of the bistability window. Conversely, an increase in the KM channels conductance resulted in a reduction in the size of the bistability window. A significant distinction between these two channels is the sign of their differential conductance (Fig. 6A, bottom, and Fig. 6B, bottom). The positive differential conductance exhibited by the KM current around the spike threshold may thus cause the weakening of bistability. To address this question, we analyzed the separate contribution of the inward and outward currents of KM on the bistability window and its resting potentials (\bar{V}), by artificially blocking one of them at a time. A similar analysis was conducted to examine the inward and outward contributions of the Kir current and to contrast them with those of the KM current.

To isolate the contribution of the inward KM current, the outward current was blocked, resulting in a zero current for potentials above E_K (Fig. 7A, left). After this adjustment, the bistability window was located in the fI curve plot for a range of inward KM current conductance $\bar{g}_{KM,inward}$ (Fig. 7A, center). Additionally, we simulated hyperpolarizing steps of current in the bistability window (between I_2 and I_1), obtained for a single value of $\bar{g}_{KM,inward}$ (Fig. 7A, right). Taken together, these results the inward KM current did not alter calcium-induced

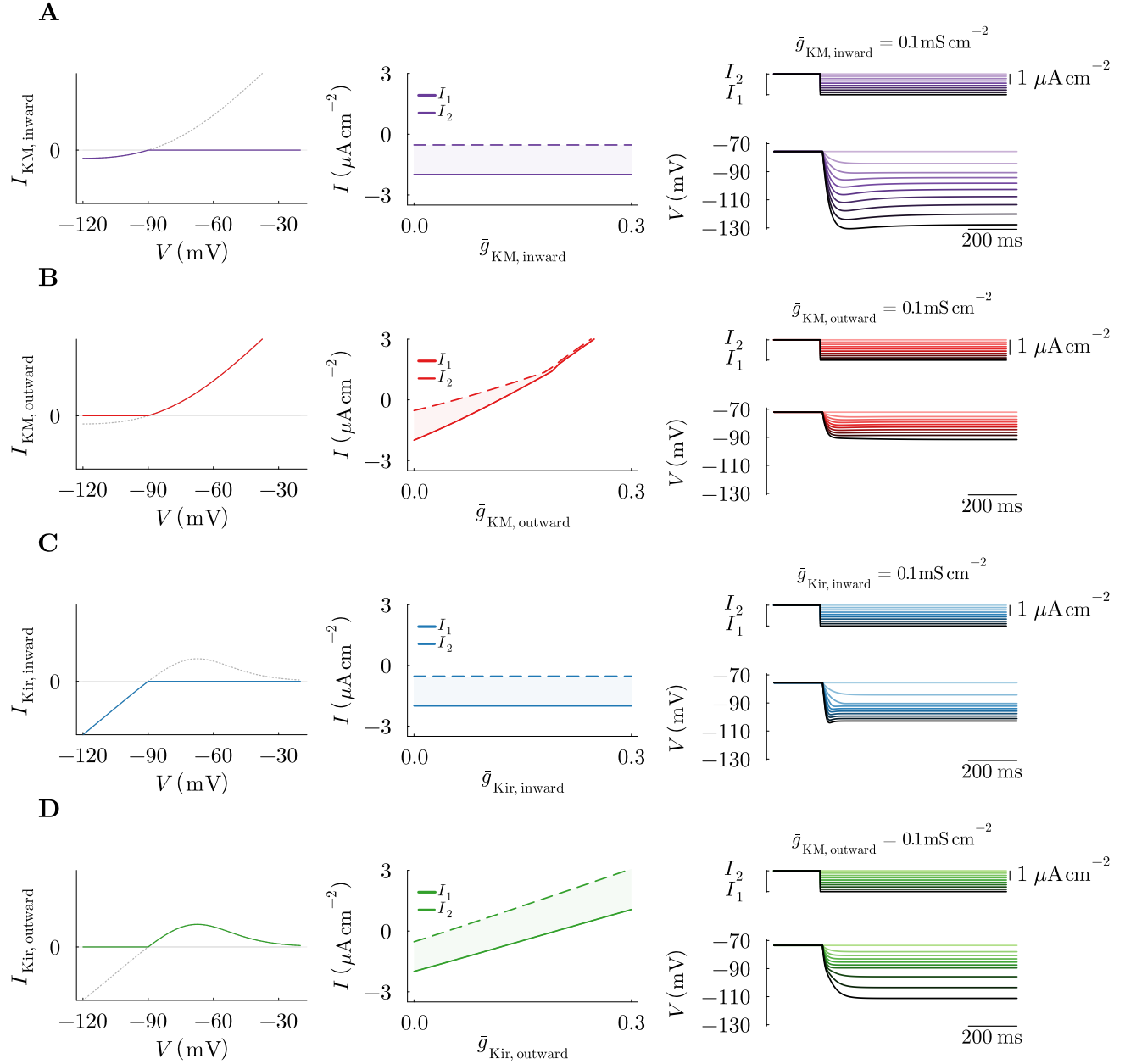


Figure 7: The inward and outward currents flowing through KM and Kir channels have different effects on the bistability window and its range of equilibrium potentials. **A**, The steady-state KM current, with a blocked outward current (left), allowing the analysis of the contribution of the inward KM current alone on the evolution of the bistability window limits, I_1 and I_2 , for an increasing inward KM current conductance $\bar{g}_{KM, inward}$ (center). Hyperpolarizing steps of currents from I_2 to I_1 showing the range of equilibrium potentials spanned in the bistability window with a fixed $\bar{g}_{KM, inward}$ (right). **B**, Same as A but with a blocked inward current, allowing the analysis of the contribution of the outward KM current alone, considering an outward KM current conductance $\bar{g}_{KM, outward}$. **C**, Same as A but with a steady-state Kir current, with a blocked outward current, allowing the analysis of the contribution of the inward Kir current. **D**, Same as C but with a blocked inward current, allowing the analysis of the contribution of the outward Kir current alone, considering an outward Kir current conductance $\bar{g}_{Kir, outward}$.

bistability and rectified slightly the resting equilibrium potentials up to E_K . Higher equilibrium potentials were not altered by this current. Conversely, the contribution of the outward KM current was isolated by blocking the inward current, which was non-zero for potentials above E_K (Fig. 7B, left). Once again, we located the bistability window for a range of outward KM conductance ($\bar{g}_{KM,outward}$) values. This analysis demonstrated that the bistability window was narrowed after an increase in the outward KM conductance (Fig. 7B, center). Finally, we simulated hyperpolarizing steps of currents between I_2 and I_1 , with a fixed $\bar{g}_{KM,outward}$ (Fig. 7B, right). The rectification of resting potentials appeared to be very efficient. This effect is in part due to the reduction in the bistability window size, as observed in Fig. 2C.

Kir channels differ from the other classes of potassium channels by their unique steady-state current shape, exhibiting a negative slope region, associated with a negative differential conductance. As for calcium channels, this feature might be responsible for maintaining and shifting the bistability window as the conductance of Kir channels increases. To address this question, we analyzed the separate contribution of the inward and outward Kir currents. Blocking the outward current isolated the contribution of the inward Kir current, which was zero for potentials above E_K (Fig. 7C, left). As the inward Kir current conductance ($\bar{g}_{Kir,inward}$) increased, the corresponding bistability window size and position remained unchanged (Fig. 7C, center). The application of hyperpolarizing steps of current between the bistability window limits (I_2 and I_1) for a single value of $\bar{g}_{Kir,inward}$ showed that the inward Kir current rectified efficiently the resting equilibrium potentials up to E_K (Fig. 7C, right). Thus, as for the inward KM current, the inward Kir current did not interfere with the bistability window, and only rectified the resting potentials up to E_K . However, the rectification provided by the inward Kir current was much more efficient, due to the high amplitude of its steady-state current. Conversely, blocking the inward current isolated the contribution of the outward Kir current, which was non-zero for potentials above E_K (Fig. 7D, left). To understand its impact on excitability, we located the bistability window in the fI curve obtained considering a range of outward Kir current conductance $\bar{g}_{Kir,outward}$ (Fig. 7D, center). Then, for a single value of $\bar{g}_{Kir,outward}$, we simulated hyperpolarizing steps of currents in the corresponding bistability window (Fig. 7D, right). On the one hand, the bistability window was clearly shifted and maintained as the outward conductance increased. On the other hand, only equilibrium potentials above E_K were rectified. Lower equilibrium values could not be rectified by the outward current because it was zero in this range of potentials.

Altogether, these analyses demonstrated that the inward current flowing in Kir and KM channels only rectified equilibrium potentials to bring them closer to E_K . Because the spike threshold was about -65 mV, the inward currents did not interfere with spiking and only altered the resting states. An additional rectification of a range

of equilibrium potentials that were in between E_K and about -70 mV was carried by the outward Kir and KM currents. The outward Kir current also provided a dynamic component that interfered with spiking and enhanced bistability. This was completely different from the contribution of the outward KM current, which highly reduced bistability. The primary distinction between these two outward potassium currents is the slope of their steady-state current and the fact that Kir (resp. KM) has a region of negative (resp. positive) differential conductance around the spike threshold. These findings suggest that the sign of an ionic current differential conductance around the spike threshold may serve as an indicator of their impact on bistability.

CaL and Kir channels facilitate the generation of plateau potentials, whereas KM channels induce a distinct excitability switch.

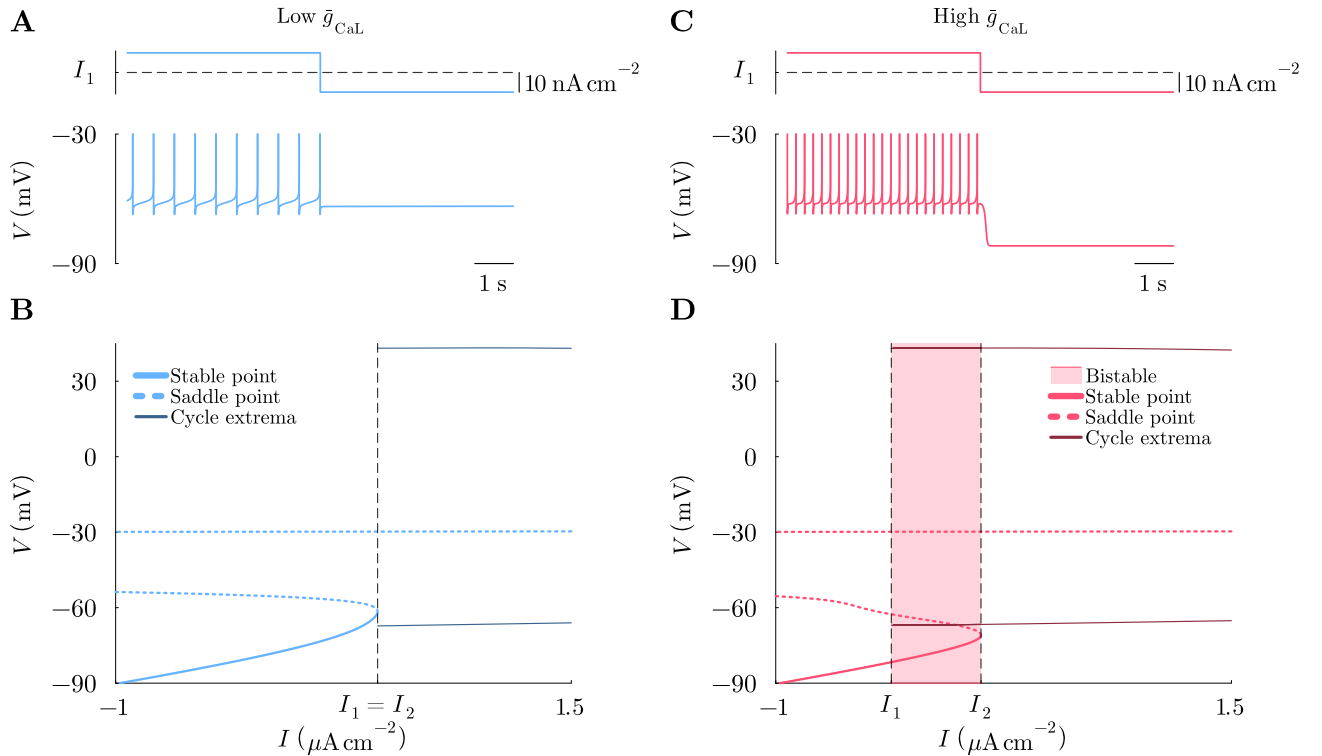


Figure 8: Identification of the excitability switch between tonic firing and plateau potentials for an increasing \bar{g}_{CaL} and a constant \bar{g}_{Kir} through bifurcation analysis. **A**, Response of the low \bar{g}_{CaL} model to an hyperpolarizing step of current down crossing I_1 . **B**, Bifurcation diagram of the low \bar{g}_{CaL} model. **C**, Same as A for an increased \bar{g}_{CaL} . **D**, Same as B for an increased \bar{g}_{CaL} .

For a given \bar{g}_{Kir} , the level of bistability increased as \bar{g}_{CaL} increased (Fig. 3E). However, the calcium channels conductance must be high enough for bistability to arise. Indeed, for low values of \bar{g}_{CaL} , the model was not bistable and showed either resting or spiking depending on the applied current value, regardless of the initial conditions (Fig. 3E, white area under the grey line). The resting potentials at I_1 also appeared to be higher in this

region, compared to their value when \bar{g}_{CaL} became higher. These results indicate that the recruitment of calcium channels at the neuronal membrane might result in an excitability switch. Similarly, a high level of recruitment of KM channels at the neuronal membrane for a given calcium channels conductance markedly reduced the level of bistability (Fig. 3B). Also, the resting potentials at I_1 are considerably elevated in comparison to those observed before an augmentation in KM channels conductance (Fig. 3C). Consequently, the recruitment of KM channels may result in a different type of excitability switch, creating the trade-off observed between bistability window size and the rectification of its equilibrium potentials. The present section examines the potential excitability switches, with a focus on the combination of Kir and CaL channels on one hand and KM and CaL channels on the other.

Firstly, we considered the potential excitability switch observed when a low calcium channels conductance was increased, for a constant Kir channels conductance of approximately 0.05 mS/cm^2 . Given that the resting-to-spiking transition is at I_1 , a neuron that initially spiked at a current above I_1 transitioned to resting after applying a hyperpolarizing step below I_1 (Figs. 8A and C). When \bar{g}_{CaL} was low, the resting potential observed lay in the range of potentials covered by spiking (Fig. 8A). After a significant increase in \bar{g}_{CaL} , the neuron became bistable, and a plateau appeared when hyperpolarizing below I_1 , outside of the bistability window (Fig. 8C). This plateau represented a clear separation between the range of potentials encompassed by spiking and the resting potentials. The bifurcation diagrams associated with each set of conductances, with respect to the applied current, offered a more comprehensive view of the existence of plateau behaviors as this current changed. Using the first set of conductances, the bifurcation diagram confirmed that the resting potentials (*i.e.*, the stable equilibria) near I_1 were within the range of potentials covered by spiking, as they exceeded the minimum value of the limit cycles displayed during spiking (Fig. 8B). This graph also highlighted the overlap between I_1 and I_2 , resulting from the absence of bistability as spiking appeared once resting disappears. For the second set of conductances, the bifurcation diagram revealed that the separation between resting potentials and spiking persisted in the entire range of current covered by the bistability window (Fig. 8D). The stable equilibrium associated with a resting state disappeared at I_2 and left room for spiking only. In both sets of conductance chosen, the resting state disappeared at I_2 through a saddle-node (SN) bifurcation, created by the collision between the stable equilibrium and a saddle point as the current increased. However, when \bar{g}_{CaL} was low, this saddle-node bifurcation occurred on an invariant circle (capturing the model trajectory during spiking). As a result, spiking appeared as soon as resting disappeared (Fig. 8B). This behavior is characteristic of a Saddle-Node on Invariant Circle (SNIC) bifurcation. This bifurcation transformed into a separate SN bifurcation at I_2 and a saddle-homoclinic (SH) bifurcation at I_1 as \bar{g}_{CaL} grew (Fig. 8D). Therefore, the excitability switch between these two cases appeared when bistability became positive,

where the SNIC bifurcation split into a SN bifurcation and a SH bifurcation (Figs. 3E and F, grey lines).

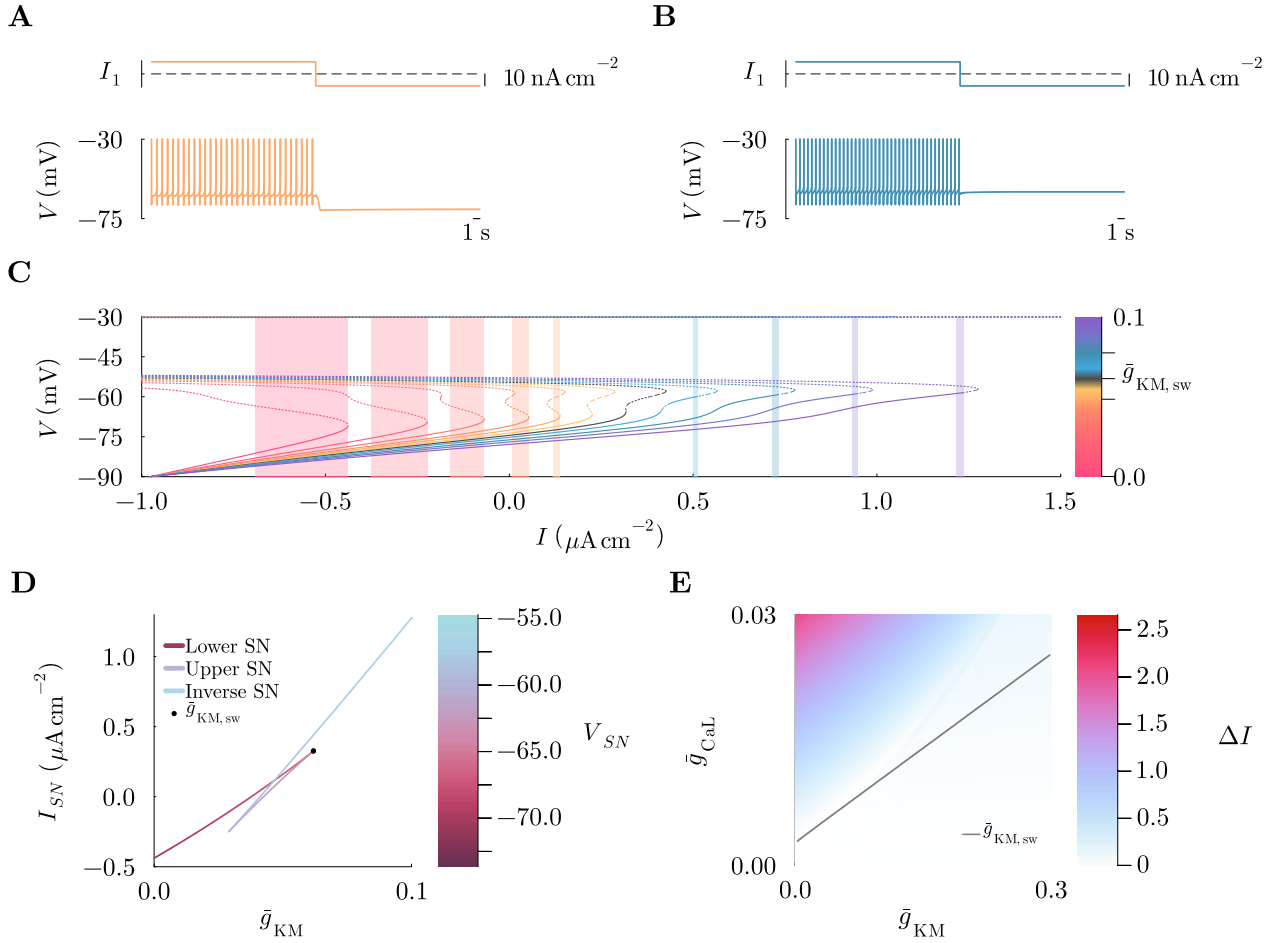


Figure 9: Identification of the excitability switch between plateau potentials and tonic firing for an increasing \bar{g}_{KM} through bifurcation analysis. **A**, Response to an hyperpolarizing step of current down crossing I_1 for an subthreshold \bar{g}_{KM} . **B**, Same as **A** for a suprathreshold \bar{g}_{KM} . **C** Bifurcation diagrams with an increasing \bar{g}_{KM} from left to right, with a fixed \bar{g}_{CaL} . Each color representing data used in **A**, **B**, and **C** corresponds to a fixed value of \bar{g}_{KM} between 0 and 0.1 according to the color gradient used in **C**. Bistability windows in **C** are represented as shaded areas and pairs of limit cycle extremes are omitted to lighten the figure. Saddle nodes and unstable nodes are represented as dotted and dashed lines, respectively. **D**, Position of the SN bifurcations displayed in **C** as a function of \bar{g}_{KM} , for a fixed \bar{g}_{CaL} . The color gradient indicates the membrane potential at which the SN bifurcation is found and allows to distinguish the 3 SNs for a range of \bar{g}_{KM} . The threshold value $\bar{g}_{KM,sw}$ denotes the excitability switch, where the lower SN collides with the inverse SN. **E**, Boundary between plateau potentials and tonic firing, superimposed on the level of bistability observed for several conductance pairs (\bar{g}_{CaL} , \bar{g}_{KM}).

Secondly, we investigated the potential excitability switch observed when a low KM channels conductance was increased, for a fixed calcium channels conductance of approximately 0.0075. To do so, we applied a hyperpolarizing current step down-crossing I_1 to two sets of conductances, with a low and a high \bar{g}_{KM} respectively. With a low value of \bar{g}_{KM} , the hyperpolarizing current step revealed a plateau that separated spiking from the resting state (Fig. 9A). Conversely, the same experiment with a high \bar{g}_{KM} showed the disappearance of such plateau (Fig. 9B).

Thus, the conductance value $\bar{g}_{KM,sw}$ at which the excitability switch occurred must be within the range of \bar{g}_{KM} tested. Bifurcation analysis was used next to properly define this threshold and to show how an increasing \bar{g}_{KM} breaks bistability.

As \bar{g}_{KM} increased, the saddle-node (SN) bifurcation extended towards higher currents (Fig. 9C, red and dark orange). This is a direct effect of amplifying any potassium current. In fact, for potentials above E_K , these currents give rise to an additional outward current that must be compensated to eliminate the resting state. In addition, \bar{g}_{KM} and \bar{g}_{CaL} together triggered high-dimensional interactions that resulted in multiple SN bifurcations (Fig. 9C, light orange to black). Nevertheless, these complex interactions manifested themselves for certain balances between \bar{g}_{KM} and \bar{g}_{CaL} . Indeed, for high \bar{g}_{KM} only a single SN bifurcation was observed (Fig. 9C, light blue to purple). Specifically, the appearance and disappearance of the two additional SN bifurcations were marked by an upper and lower inflection point, respectively, in the bifurcation diagram (Fig. 9C, dark orange and black). They created an interesting interlude within which the SN bifurcation switched from lower to upper state, from low to high \bar{g}_{KM} , that inherently changed excitability. Indeed, the bifurcation diagram for the same \bar{g}_{KM} as in Fig 9A showed both a lower SN bifurcation and a separate SH bifurcation (Fig. 9C, light orange with a shaded area). Thus, when hyperpolarizing around the SH bifurcation current, the neuron response exhibited a plateau as the resting potentials around this current were significantly lower than the range of potentials covered by spiking. Conversely, the bifurcation diagram corresponding to a higher \bar{g}_{KM} showed that the resting state was significantly higher and close to an upper SN bifurcation, and disappeared by becoming unstable (Fig. 9C, light blue). Therefore, the stable equilibrium associated with resting disappeared earlier than the collision with the saddle point, by becoming unstable, through a Hopf bifurcation. For a small range of \bar{g}_{KM} between those used to represent these two behaviors, it was also possible to observe tonic firing based on a SNIC bifurcation (Fig. 9C, yellow and black), similar to Fig. 8A.

These deformations of the bifurcation diagram narrowed the bistability windows (Fig. 9C, shaded areas). As \bar{g}_{KM} increased, the bistability window became smaller because the SH bifurcation and the SN bifurcation delimiting it came closer together. At some point, bistability disappeared because these two bifurcations combined to form a SNIC bifurcation (Fig. 9C, yellow). At the value $\bar{g}_{KM,sw}$, the lower SN bifurcation disappeared (Fig. 9C, black). For a slightly higher \bar{g}_{KM} , only the upper SN bifurcation remained (Fig. 9C, light blue). A small region of bistability lay near the upper SN, but this bistability window upper limit was located at the Hopf bifurcation and not at the SN bifurcation.

With the conductance \bar{g}_{CaL} chosen, a range of \bar{g}_{KM} allowed to find 3 SN bifurcations instead of a single one (Fig. 9D). Each limit of this range corresponds to an inflection point in the bifurcation diagram. Depending on

its relative position with the remaining SN bifurcation, the inflection point deformed to create an inverse SN, pointing towards lower currents, and an upper (resp. lower) SN bifurcation as \bar{g}_{KM} increased (resp. decreases). The value $\bar{g}_{KM,sw}$ creating the lower inflection point set the excitability switch. Indeed, above this value, the resting potentials were in the range covered by spiking, and disappeared through a Hopf bifurcation. The resulting firing pattern observed was Hopf-type tonic firing. This singular value $\bar{g}_{KM,sw}$, which lay at the transition between two very different types of excitability, represented a high-dimensional transcritical bifurcation. This excitability switch can be tracked for a range of \bar{g}_{CaL} (as represented in Fig. 9E).

On the whole, these results showed that the combination of Kir and CaL channels favors bistability and plateau-type behavior. Both of these channels promote the separation between the SN bifurcation and the SH bifurcation, which in turn increases the distance between I_2 and I_1 . In contrast, KM and CaL currents compete for their preferred type of excitability. The transition from plateau to tonic excitability occurs due to high dimensional interactions, probably resulting from the coupling of opposite differential conductances operating on a very slow timescale.

Discussion (1500 Words Maximum)

Under the right modulatory conditions, deep dorsal horn projection neurons can switch from tonic firing to plateau potentials, with sustained afterdischarges (Derjean et al. (2003)). This behavior suggests that their intrinsic properties, in response to neuromodulation, may generate robust bistability, a fundamental feature underlying the occurrence of sustained afterdischarges. In this study, we used a conductance-based model to investigate how two different couples of ion channels can create plateau potentials and robust bistability. Our results demonstrated that the simultaneous increase in the conductances of L-type calcium (CaL) channels and inward rectifier potassium (Kir) channels enhances both plateau potentials and robust bistability. Unlike other potassium channels, we show that Kir channels promote bistability through their unique steady-state current shape. The cooperation between CaL and Kir channels represents a candidate pathway to enhance projection neuron activity, amplifying nociception during central sensitization.

Unlike classical voltage-gated potassium channels, Kir channels strengthen bistability when combined with CaL channels. To understand this effect, we investigated the contributions of Kir channels to bistability by blocking either the outward or the inward Kir current. This analysis revealed that, on the one hand, the outward Kir current enhances the size of the bistability window—the range of currents at which both resting and spiking exist—and shifts it towards higher currents as its maximal conductance increases. On the other hand, the inward Kir current only rectifies the resting equilibrium potentials up to their reversal potential, E_K . Therefore, in line with Amarillo

et al. (2018), we support that the ability of Kir channels to enhance bistability must originate from the singular shape of their outward steady-state current, which is markedly distinct from those of classical types of voltage-gated potassium channels. The same analysis was conducted with M-type potassium (KM) channels, which open at a similar timescale as Kir channels but differ in the shape of their steady-state current. The results showed that the outward KM current is responsible for reducing the size of the bistability window. Additionally, the inward KM current exhibited a rectification of resting equilibrium potentials, although this was less pronounced than that observed with the inward Kir current. These results suggest that the shape of these steady-state outward currents captures their effect on bistability, while both KM and Kir currents increase the current range at which bistability can be observed.

Modulatory inputs may alter the range of currents in which bistability exists, which could result in long-lasting afterdischarges to a greater or lesser extent. The occurrence of long-lasting afterdischarges is highly dependent on the input currents and their relative position to the bistability window. Long-lasting afterdischarges appear after applying an input current pulse only if its baseline current is within the range of the bistability window. Therefore, if the baseline and amplitude of a pulse of current are constant, long-lasting afterdischarges may become less frequently observed if the bistability window limits increase (e.g., if the Kir channels conductance increases). In that case, the baseline current may become lower than the limits of the bistability window, which would prevent long-lasting afterdischarges from occurring. Conversely, if modulatory inputs shift the limits of the bistability window to lower values (e.g., if the Kir channels conductance decreases), long-lasting afterdischarges may become more frequently observed. Those results align with the experimental results reported in Derjean et al. (2003). However, it seems reasonable to assume that long-lasting afterdischarges and persistent firing may eventually cease *in vivo*. In such a scenario, robust bistability could be combined with additional mechanisms at the single-cell or network level, operating on a slower timescale than Kir channels, that terminate long-lasting afterdischarges.

The strong bistability created following the simultaneous increase in both CaL and Kir channels conductances results in the generation of plateau potentials and long-lasting afterdischarges robust to perturbations in input current and intrinsic variability. After applying Normal noise superimposed on the input applied current, the neuron was able to maintain its initial state (resting or spiking) as long as the noisy input current magnitude remained within the limits of the bistability window, which can be of the order of $1 \mu\text{A}/\text{cm}^2$. Moreover, this experiment revealed that the resting state can withstand higher perturbations than the spiking state at the center current of the bistability window. This suggests that resting is a functional state that is more robust than spiking when the input current is corrupted by noise. Such behavior seems relevant in pain processing, as the neuron

tends to be silent rather than transferring spikes if corrupted by noisy input signals. Furthermore, our results showed that the bistability arising from the combination of CaL and Kir channels is bounded within $\pm 10\%$ of their nominal value when exposed to intrinsic variability of 30% . This suggests that this type of bistability remains reliable when considering a heterogeneous population of neurons. Therefore, CaL and Kir channels may provide a reliable pathway targeted during central sensitization. In a broader sense, Kir channels may serve as a fundamental component in the establishment of a rudimentary form of memory at the single-cell level, particularly in other functions of the nervous system where the storage of contextual information is of fundamental importance (Sanders et al. (2013); Amarillo et al. (2018); Delmoe and Secomb (2023)).

This study used a conductance-based model to demonstrate that robust and physiological bistability emerges when L-type calcium channels (CaL) are combined with inward rectifier potassium (Kir) channels. The cooperation between these two types of channels is such that they shift the current range in which bistability is observed (*i.e.*, the bistability window) in opposite directions, but at the same time both strengthen it by increasing its size. We propose that this cooperation relies on a common principle: the existence of a region of negative slope in the steady-state currents around the spike threshold. Evidence supported that the emerging bistability is robust to intrinsic variability and to noise superimposed on the input current. Furthermore, the type of bistability examined in this study is manifested by the appearance of plateau potentials, combined with sustained afterdischarges. The synergic increase in CaL and Kir conductances may represent a potential pathway targeted during central sensitization to switch the functional state of nociception.

References

- Amarillo Y, Tisone AI, Mato G, Nadal MS (2018) Inward rectifier potassium current I_{kir} promotes intrinsic pacemaker activity of thalamocortical neurons. *Journal of Neurophysiology* 119:2358–2372.
- Borges F, Protachevitz P, Souza D, Bittencourt C, Gabrick E, Bentivoglio L, Szezech J, Batista A, Caldas I, Duran-Bernal S, Pena R (2023) The Roles of Potassium and Calcium Currents in the Bistable Firing Transition. *Brain Sciences* 13:1347.
- Brewer CL, Baccei ML (2018) Enhanced Postsynaptic GABAB Receptor Signaling in Adult Spinal Projection Neurons after Neonatal Injury. *Neuroscience* 384:329–339.
- Cata J, Weng HR, Chen JH, Dougherty P (2006) Altered discharges of spinal wide dynamic range neurons

- and down-regulation of glutamate transporter expression in rats with paclitaxel-induced hyperalgesia. *Neuroscience* 138:329–338.
- Crunelli V, Tóth TI, Cope DW, Blethyn K, Hughes SW (2005) The ‘window’ T-type calcium current in brain dynamics of different behavioural states. *The Journal of Physiology* 562:121–129.
- Delmoe M, Secomb TW (2023) Conditions for Kir-induced bistability of membrane potential in capillary endothelial cells. *Mathematical Biosciences* 355:108955.
- Derjean D, Bertrand S, Le Masson G, Landry M, Morisset V, Nagy F (2003) Dynamic balance of metabotropic inputs causes dorsal horn neurons to switch functional states. *Nature Neuroscience* 6:274–281.
- Destexhe A, Contreras D, Sejnowski TJ, Steriade M (1994) A model of spindle rhythmicity in the isolated thalamic reticular nucleus. *Journal of Neurophysiology* 72:803–818.
- Dovzhenok A, Kuznetsov AS (2012) Exploring Neuronal Bistability at the Depolarization Block. *PLoS ONE* 7:e42811.
- Drion G, Franci A, Dethier J, Sepulchre R (2015) Dynamic Input Conductances Shape Neuronal Spiking. *eneuro* 2:ENEURO.0031–14.2015.
- Engbers JD, Fernandez FR, Turner RW (2013) Bistability in Purkinje neurons: Ups and downs in cerebellar research. *Neural Networks* 47:18–31.
- Ford NC, Baccei ML (2016) Inward-rectifying K⁺ (Kir2) leak conductance dampens the excitability of lamina I projection neurons in the neonatal rat. *Neuroscience* 339:502–510.
- Franci A, Drion G, Seutin V, Sepulchre R (2013) A Balance Equation Determines a Switch in Neuronal Excitability. *PLoS Computational Biology* 9:e1003040.
- Kazantsev VB, Asatryan SY (2011) Bistability induces episodic spike communication by inhibitory neurons in neuronal networks. *Physical Review E* 84:031913.
- Latremoliere A, Woolf CJ (2009) Central Sensitization: A Generator of Pain Hypersensitivity by Central Neural Plasticity. *The Journal of Pain* 10:895–926.
- Le T, Verley DR, Goaillard JM, Messinger DI, Christie AE, Birmingham JT (2006) Bistable Behavior Originating in the Axon of a Crustacean Motor Neuron. *Journal of Neurophysiology* 95:1356–1368.

- Lee RH, Heckman CJ (1998) Bistability in Spinal Motoneurons In Vivo: Systematic Variations in Rhythmic Firing Patterns. *Journal of Neurophysiology* 80:572–582.
- Malcangio M (2018) GABAB receptors and pain. *Neuropharmacology* 136:102–105.
- Monteiro C, Lima D, Galhardo V (2006) Switching-on and -off of bistable spontaneous discharges in rat spinal deep dorsal horn neurons. *Neuroscience Letters* 398:258–263.
- Murata Y, Yasaka T, Takano M, Ishihara K (2016) Neuronal and glial expression of inward rectifier potassium channel subunits Kir2.x in rat dorsal root ganglion and spinal cord. *Neuroscience Letters* 617:59–65.
- Naudin L, Raison-Aubry L, Buhry L (2023) A general pattern of non-spiking neuron dynamics under the effect of potassium and calcium channel modifications. *Journal of Computational Neuroscience* 51:173–186.
- Reali C, Russo RE (2005) An integrated spinal cord–hindlimbs preparation for studying the role of intrinsic properties in somatosensory information processing. *Journal of Neuroscience Methods* 142:317–326.
- Robinson CR, Zhang H, Dougherty PM (2014) Altered discharges of spinal neurons parallel the behavioral phenotype shown by rats with bortezomib related chemotherapy induced peripheral neuropathy. *Brain Research* 1574:6–13.
- Sanders H, Berends M, Major G, Goldman MS, Lisman JE (2013) NMDA and GABAB (KIR) Conductances: The “Perfect Couple” for Bistability. *Journal of Neuroscience* 33:424–429.
- Shoemaker PA (2011) Neural bistability and amplification mediated by NMDA receptors: Analysis of stationary equations. *Neurocomputing* 74:3058–3071.
- Woolf CJ (2010) What is this thing called pain? *Journal of Clinical Investigation* 120:3742–3744.
- Yuen GL, Hockberger PE, Houk JC (1995) Bistability in cerebellar Purkinje cell dendrites modelled with high-threshold calcium and delayed-rectifier potassium channels. *Biological Cybernetics* 73:375–388.
- Zain M, Bonin RP (2019) Alterations in evoked and spontaneous activity of dorsal horn wide dynamic range neurons in pathological pain: a systematic review and analysis. *Pain* 160:2199–2209.